



POLITECNICO
MILANO 1863

DIPARTIMENTO DI
INGEGNERIA CIVILE E AMBIENTALE

Bark Beetle Detection Through Satellite Hyperspectral Derived Vegetation Indexes on Spectral Unmixed Trees

TESI DI LAUREA MAGISTRALE IN
GEOINFORMATICS ENGINEERING -
INGEGNERIA GEOINFORMATICA

Author: **Alessandro Austoni**

Student ID: 976780

Advisor: Prof. Maria Antonia Brovelli

Co-advisors: Daniele Oxoli

Academic Year: 2022-23

Abstract

The bark beetle, a destructive insect pest, poses a significant threat to forests worldwide. Over the past few decades, the incidence and severity of bark beetle attacks on trees (especially spruce and pine trees) have increased due to the effects of climate change, leading to substantial economic and ecological consequences. These tiny insects, often attracted to weakened or stressed trees, infest and feed on the inner bark, disrupting the tree's nutrient transport system and ultimately resulting in widespread tree mortality. Detecting unhealthy trees and limiting the effects of the parasite on the vegetation is crucial to prevent the infestation to spread. This is why remote sensing plays a crucial role in Bark Beetle detection, often used in synergy with ground surveys. These analyses are usually carried out by aerial Hyperspectral inspections, which need to be properly scheduled and planned ahead of time, entailing significant costs and efforts. The presented study aims at developing a free alternative solution to the usual aerial Bark Beetle detection, using Hyperspectral satellite data from the PRISMA sensor. Satellite data coming from this sensor has not only free access and greater temporal availability, but it allows to perform analyses over a broader land extension at the cost of a lower spatial resolution. The first part of the analysis includes most of the innovative aspects, as it implies the extraction of trees' crowns from satellite data through an Unmixing procedure that relies on aerial spectral signatures. The second one, involves the assessment of the Beetle attack's risk, through the computation of spectral vegetation indexes over the trees' areas extracted from the Unmixing step. The algorithm is calibrated on aerial data of a specific area and tested over a completely different land sector. Once calibrated, Thanks to the complete availability of satellite data, the procedure can be applied to any other area of interest, proving the scalability of the study. The results are provided in the form of binary masks, supplying insights on the zones subjected to the highest risk of infestation. The outcomes of the analysis have proven good signs of compatibility between aerial and satellite data, however, some issues emerged from the significant difference in spatial resolution between the aerial and satellite sensor. Nevertheless, the possibility of extending the analysis over several kilometres of land with limited to no costs makes the new satellite algorithm an important strategical help in the planning of more precise aerial and ground surveys.

Keywords: Hyperspectral, Bark Beetle, Spectral Unmixing, Vegetation Indexes, Remote Sensing, Forests

Abstract in lingua italiana

Il Bostrico, un insetto nocivo distruttivo, rappresenta una minaccia significativa per le foreste di tutto il mondo. Negli ultimi decenni l'incidenza e la gravità degli attacchi del Bostrico sugli alberi (soprattutto abeti e pini) sono aumentate a causa degli effetti del cambiamento climatico, con notevoli conseguenze economiche ed ecologiche. Questi minuscoli insetti, spesso attratti da alberi indeboliti o in condizioni di stress, infestano e si nutrono della corteccia interna, interrompendo il sistema di trasporto dei nutrienti dell'albero e provocando infine una diffusa mortalità degli alberi. Individuare alberi sotto attacco del parassita e limitarne gli effetti è fondamentale per evitare che l'infestazione si diffonda. Ecco perché il telerilevamento gioca un ruolo cruciale nella rilevazione del Bostrico, spesso utilizzato in sinergia con i rilievi a terra. Queste analisi vengono solitamente effettuate mediante ispezioni aeree iperspettrali, che devono essere opportunamente programmate e pianificate in anticipo, comportando costi e sforzi significativi per le aziende. Il presente studio mira a sviluppare una soluzione alternativa gratuita al consueto rilevamento aereo del Bostrico, utilizzando i dati satellitari iperspettrali del sensore PRISMA. I dati satellitari di questo sensore non solo sono di libero accesso e dispongono di maggiore disponibilità temporale, ma consentono di eseguire analisi su un'estensione territoriale più ampia, al costo di una risoluzione spaziale inferiore. La prima parte dell'analisi comprende la maggior parte degli aspetti innovativi, in quanto include l'estrazione delle chiome degli alberi dai dati satellitari attraverso una procedura di Unmixing che si basa su firme spettrali aeree. La seconda, invece, prevede la valutazione del rischio di attacco del parassita, attraverso il calcolo degli indici spettrali di vegetazione sulle aree arboree estratte nella fase di Unmixing. L'algoritmo è calibrato su dati aerei di un'area specifica e testato su un'area completamente diversa. Grazie alla completa disponibilità dei dati satellitari, una volta calibrata, la procedura può essere applicata a qualsiasi altra area di interesse e questo ne dimostra la scalabilità. I risultati sono forniti sotto forma di maschere binarie, le quali individuano le zone soggette a maggior rischio di infestazione. Durante lo studio sono emerse alcune difficoltà dovute alla significativa differenza di risoluzione spaziale tra il sensore aereo e quello satellitare, ma la possibilità di estendere l'analisi su diversi chilometri di terreno, rende questo nuovo algoritmo satellitare un importante aiuto

strategico nella progettazione di più precise misurazioni aeree e terrestri.

Parole chiave: Telerilevamento Iperspettrale, Bostrico, Spectral Unmixing, Indici di Vegetazione, Foreste

Contents

Abstract	i
Abstract in lingua italiana	iii
Contents	v
1 Introduction	1
2 State of the art	5
2.1 Useful indexes in Bark Beetle’s detection	5
2.1.1 Infrared and red-edge indexes	5
2.1.2 Leaf and Water indexes	7
2.1.3 Tasseled-cap indexes	9
2.1.4 Other indexes	10
2.2 Techniques for Spectral Unmixing in Remote Sensing	11
3 Material and Methods	17
3.1 Sensors and Data	17
3.2 Pre-Processing	22
3.2.1 PRISMA data pre-processing	23
3.2.2 asiaFENIX data pre-processing	26
3.3 Spectral Unmixing	26
3.3.1 AsiaFENIX image spectral unmixing	28
3.3.2 PRISMA image spectral unmixing	31
3.4 Vegetation Indexes Extraction	33
3.4.1 Threshold extraction on asiaFENIX data	34
3.4.2 Index binary map production from PRISMA data	35
3.5 Frequency Analysis	36
3.6 Validation	37

4	Results and comments	39
4.1	Pre-Processing results	39
4.2	Unmixing results	42
4.3	Spectral Indexes Extraction results	53
4.4	Frequency Analysis results	56
4.5	Validation results	59
5	Conclusions and future improvements	63
	Bibliography	65
	List of Figures	69
	List of Tables	73

1 | Introduction

Hyperspectral imaging is becoming common practice in the remote sensing field. Nowadays, Earth Observation can benefit from the advantage of having denser bands in the spectrum, that can provide better and well-defined spectral signatures, helping in the detection of more material types on the ground. The need of having higher spectral resolution sensors was born around 1970 when geologists found that many mineral morphological features weren't correctly detected by the few bands of Landsat MSS (Multispectral Scanner System). It was during this period that airborne Hyperspectral sensors started to be developed as precursors of the newer satellite or spaceborne cameras [27].

Bark beetle is nowadays a relevant source of concern for trees' health, as the increasing effects of climate change are improving the European spruce bark beetle life condition, most of the trees in the whole European area are now in danger.

When this insect attacks, it spreads a chemical substance that attracts thousands of other beetles, that can potentially kill a tree. The freezing cold of winter is supposed to act against this insect and kill most of its own kind, but as known climate change's warming effects, caused winter to shorten and summer to stretch, allowing more sustainable living conditions for this creature. It has also been proven that the increase in trees death causes a vicious circle to the Bark Beetle life cycle, as, once dead, a tree can release a large amount of carbon and VOC (Volatile Organic Compounds) that will contribute to climate change and thus to global warming [19] [13].

Remote sensing plays a fundamental role in the detection and prevention of Bark Beetle attacks; in particular, thanks to vegetation spectral indexes obtained from satellite data, it is possible to monitor trees' health state and thus keep track of the infection.

Once attacked by a beetle a tree goes through three different stages [10]:

- green phase: tree's needles or leaves stays green in this time period
- red phase: tree's leaves or needles turn progressively from green to yellow and then to a reddish tone
- grey phase: this is the last phase of the attack, in which the parasite has concluded

the infestation and the tree reaches its maximum level of decay towards death. Dead leaves or needles fall from branches and the bare tree stands in a grey.

The goal of this study is to evaluate trees' exposure to the parasite attack, by making use of free access hyperspectral imagery from the PRISMA (PRecurso IperSpettrale della Missione Applicativa) satellite.

Due to the small size of this insect (around 5mm) and the coarse resolution of PRISMA data (30m), it's undoubtedly unfeasible to directly detect the parasite from satellite imagery. Exactly for this reason, Bark Beetle detection is only possible through a proper assessment of its effects on trees' health, by the extraction of specific spectral vegetation indexes related to the stress state of the plant. Moreover, the mean size of a tree is still quite small to be recognized by the most common GSDs (Ground Sample Distance) of satellite data, which implies the need for an improved spatial resolution. Therefore Bark Beetle detection is a procedure, generally carried out by airborne sensors, which by being mounted on aircrafts or helicopters, are able to collect images with a very short GSD.

Nevertheless, to obtain such a high spatial resolution, aircrafts need to fly at close distances to the ground, which in turn causes a much smaller ground coverage area when compared to satellite sensing. Another drawback of airborne remote sensing concerns the costs, since those flights are often carried out as one-time operations, that need to be properly scheduled and performed on demand.

However, satellite hyperspectral imagery offers images with high coverage area at zero costs for the user, giving the possibility of continuous monitoring of the Earth in time. Of course, these benefits come with a cost: a much coarser spatial resolution.

To overcome this important boundary, this study implements an unmixing procedure, that helps satellite imagery discern trees from other features by exploiting the higher spectral and spatial resolution content of the aerial data. This allowed to build the foundations of a model able to spare time and expenses of high-cost survey planned operations and to expand, replicate and possibly improve the aerial analysis to a much wider geographical area with zero costs.

The area chosen to perform the aforementioned analysis is the Gadertal Valley (Trentino-Alto Adige, Italy).

Aerial data were used to improve satellite hyperspectral imagery for parasite detection. The aerial images used as the main reference are the outputs of an aerial survey performed by the "AVT AS Italia" company, which have been used both as training and validation datasets for this current study. The survey was carried out with the objective of monitoring the health state of the Spruce trees, present in the Gadertal forest (Northern Italy), which has been subjected to a remarkable Bark Beetle attack in the past few years.

The inspection has been performed with the "AisaFENIX" hyperspectral aerial sensor on the 8th of October 2022, by collecting images of six zones distributed over the Gadertal area (see Figure 1.1).

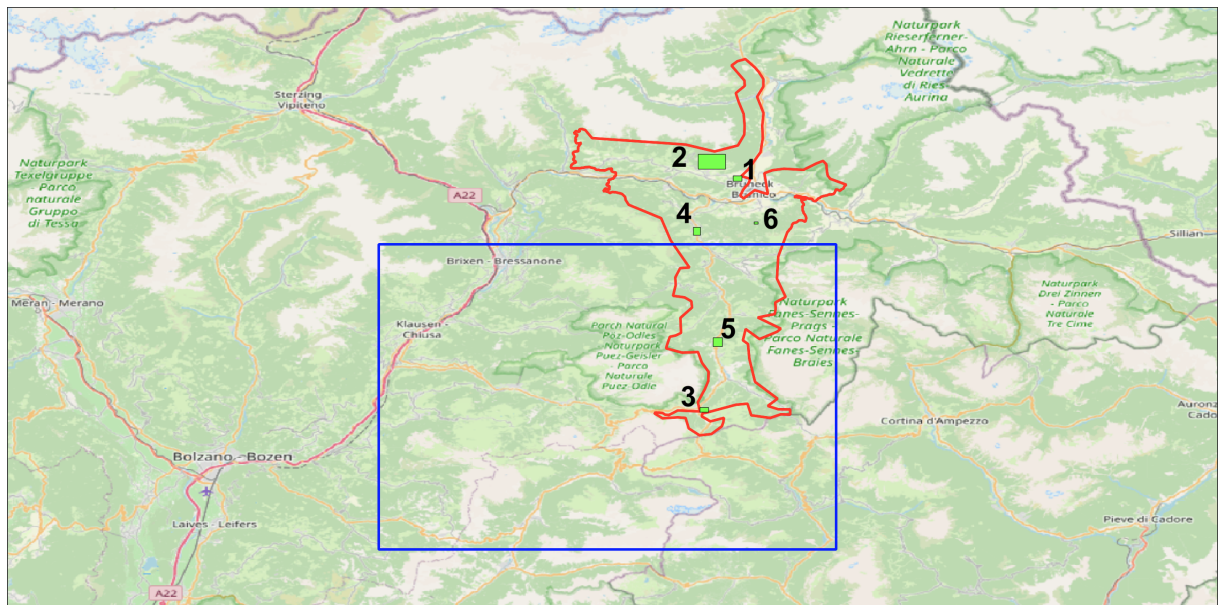


Figure 1.1: Geographical distribution of the study area and the extent of the two sensor acquisitions. In red it is possible to appreciate the Gadertal study area outline, in blue the PRISMA image outline and in green the airborne acquisitions with their corresponding area number in black

As can be appreciated from the geographical overview in Figure 1.1, just two of the six zones, happened to be completely included in a 30km x 30km square tile of the selected PRISMA acquisition. Their size is variable and depends on the way they have been cropped from the entire acquisitions stripe during the survey. Area 5 has been used to train the model and has a size of 758m x 1064m, while Area 3 has been used for validation purposes and has a size of 720m x 552m.

The results of the analysis consist mainly of binary maps, reporting areas with a high risk of attack with a value of 1 and low-risk ones with a value of 0. They were produced by computing and thresholding vegetation indexes related to the Bark Beetle effects on trees.

Despite the spatial resolution of the binary maps produced from the PRISMA satellite imagery (30m resolution), the algorithm can be potentially used as an early inspection tool, providing insights into larger portions of land and aiding the planning of further ground or aerial surveys.

The remainder of the thesis is structured as follows. First of all, in view of the research and innovative nature of this study, it is imperative to understand the current state of the art within Bark Beetle's detection, which will be the first chapter of this analysis. The second chapter is the material and methods one, which involves a comprehensive literature review, data collection, and analysis. By leveraging established theories and frameworks, combined with ad-hoc techniques implemented for this current study, the chapter aims to provide a deeper understanding of the subject matter. The results obtained from this investigation are thoroughly examined and commented upon in the third chapter, highlighting the key findings, trends, and correlations discovered. These findings form the basis for drawing meaningful conclusions and making informed recommendations, part of the last chapter. The subsequent sections of this thesis will delve into each aspect in greater detail, providing a comprehensive analysis of the research methodology, results, and their implications.

2 | State of the art

2.1. Useful indexes in Bark Beetle's detection

As anticipated in section 1, the Bark Beetle attack may happen in 3 different phases (green, red and grey). It is very important to choose the correct index for Beetle detection, in order to target the right temporal phase of the attack (the green one, which is the hardest to detect since it doesn't leave any visible sign on vegetation), and thus to design the right plan to contain the outbreak. As stated in the literature, in fact, there are several ways to mitigate insect infestation, that should be properly picked, such as pheromone trapping, burning, clearing of wind-thrown trees and selective thinning [11]. It must be considered that indexes don't directly detect the parasite's presence (which it would be impossible to be spotted only by reflectance values as well as due to the pixel resolution), but an anomalous index value may explain some stress or illness tree's condition, which could then be correlated, after a proper validation with ground truth, to the insect attack.

Once computed, indexes can be used alone or combined in groups of several indexes to assess the risk of attack. Single indexes or groups of them can be used as training inputs for different Machine Learning algorithms (SVM Support Vector Machines, Neural Networks and other Machine Learning Solutions) to produce a more articulated and targeted infestation identification. Moreover, the use of hyperspectral satellite data can possibly allow the above-mentioned algorithms to perform at higher accuracy levels with respect to the common multispectral data, thanks to its higher spectral resolution, which grants a higher precision in the spectrum while computing a larger number of indexes. In the next subsection the main indexes used in literature to detect Bark Beetle, grouped depending on the purpose for which they are employed, will be presented.

2.1.1. Infrared and red-edge indexes

In this category are included infrared indexes (Table 2.1), which help to monitor photosynthetic activity, and the most common vegetation indexes, indicators of the general

health state of the flora. As stated in [15], for example, NDVI (Normalized Difference Vegetation Index) is an index available in most multispectral satellite systems which, by making use of red and infrared bands, helps to evaluate the photosynthetic activity, which is crucial to estimate the effects of living organisms on vegetation. Infrared spectral bands are affected by several changes in reflectance values, as the stress biases vegetation's physical and chemical properties. Several examples are available in the literature, for example, [15] states that NDVI time series extracted from MODIS were able to spot tree leaf loss by gypsy moth outbreaks in eastern North America. And again, the same data products were useful to map dead trees in forests affected by mountain pine beetle attacks and droughts. In table 2.1 a list of infrared indexes, together with the involved bands and their formula is reported.

Infrared Indexes

	bands	formula
(NDII) Normalized Difference Infrared Index	833nm, 1649nm	$\frac{833-1649}{833+1649}$
(NDVI) Normalized Vegetation Index	RED, NIR	$\frac{NIR-RED}{NIR+RED}$
(TVI) Transformed Vegetation Index	NDVI	$\sqrt{NDVI + 0.5}$
(MSAVI) Modified Soil-Adjusted Vegetation Index	NIR, RED	$\frac{2NIR+1-\sqrt{(2NIR+1)^2-8(NIR-RED)}}{2}$
(NBRI) Normalized Burn Ratio Index	NIR, SWIR	$\frac{NIR-SWIR}{NIR+SWIR}$
(NRVI) Normalized Ratio Vegetation Index	RED, NIR	$\frac{\frac{NIR}{RED}-1}{\frac{NIR}{RED}+1}$
(GNDVI) Green Normalized Difference Vegetation Index	NIR, 540:570nm	$\frac{NIR-[540:570]}{NIR+[540:570]}$

Table 2.1: Infrared indexes' involved spectral bands with their formulas

In addition, red-edge indexes are used to monitor chlorophyll content (Table 2.2), so that high values in this band are strictly correlated to the infestation state of the parasite [1]. In [1], Haidi et al. were able to discriminate between healthy and infested trees sooner than other vegetation indexes, proving the effectiveness of red edge and SWIR indexes. Moreover, it has been found that red edge and SWIR bands showed successfully their

ability to detect bark beetle infestation, in both the early and late stages of the attack. Their results revealed that these indexes can potentially improve the monitoring and detection of this insect with crucial implications for European bark beetle future studies.

Red-edge Indexes

	bands	formula
(NDRE) Normalize difference red-edge index	NIR, red-edge	$\frac{NIR-rededge}{NIR+redege}$
(REIP) Red-edge inflection point	670nm, 700nm, 740nm, 780nm	$700 + 40\left(\frac{(\frac{670+780}{2})-700}{740-700}\right)$
(CLRE) Red-Edge Band Chlorophyll Index	690:720nm, 760:800nm	$\left(\frac{[760:800]}{[690:720]}\right)^{(-1)}$

Table 2.2: Red-edge indexes' involved spectral bands with their formulas

2.1.2. Leaf and Water indexes

Foliage is one of the first signs of trees' health, indeed, while the attack progresses, after the green phase, leaves start gradually changing colour (from yellow to red) in the red stage of the infestation, until they fall and lose their photosynthetic ability as well as water and chlorophyll, during the grey stage. Due to this, it is important to anticipate detection to the green stage, where infestation's effects are not visible to human sight, and plant decay proceeds unseen. This is possible also by monitoring leaves' health and stress state, through several indexes related to water content and contained biochemical substances (Table 2.3). Some of these indexes belong also to the aforementioned red-edge category, as they are computed using the same band.

Leaf and Water Indexes

		bands	formula
(WBI) Water Band Index		970nm, 900nm	$\frac{970}{900}$
(NDWI) Normalized Difference Water Index		869nm, 1240nm	$\frac{860-1240}{860+1240}$
(mNDWI) Modified Normalized Difference Water Index		green, SWIR	$\frac{green-SWIR}{green+SWIR}$
(LWCI) Leaf water content index		NIR, MIDIR	$\frac{\log(1-(NIR-MIDIR))}{-\log(1-(NIR-MIDIR))}$
(DSWI) Disease stress water index		547nm, 682nm, 802nm, 1657nm	$\frac{802+547}{682+1657}$
(CIG) Chlorophyll index green		NIR, GREEN	$\frac{NIR}{GREEN} - 1$
(GLI) Green leaf index		547nm, GREEN, RED, BLUE	$\frac{2GREEN-RED-BLUE}{2GREEN+RED+BLUE}$
(CVI) Chlorophyll vegetation index		NIR, RED, GREEN	$NIR \frac{RED}{GREEN^2}$
(PBI) Plant biochemical index		NIR, GREEN	$\frac{NIR}{GREEN}$
(SLAVI) Specific Leaf Area Vegetation Index		NIR, RED, SWIR	$\frac{NIR}{RED+SWIR}$
(MCARI) Modified Chlorophyll Absorption Ratio Index		550nm, 705nm, 750nm	$((750 - 705) - 0.2(750 - 550)) \frac{750}{705}$
(MTCI-MERIS) Terrestrial Chlorophyll Index		681nm, 709nm, 754nm	$\frac{754-709}{709-681}$

Table 2.3: Leaf and water indexes' involved spectral bands with their formulas

Moreover, bark beetle infestation is often followed by a decrease in stomatal conductance and foliage in trees, often related to droughts and moisture content (Table 2.4). The canopy conductance is a vital parameter for trees' health since it represents water vapour exchanges between vegetation and the atmosphere. In response to drought or hydraulic limitation, the canopy conductance changes the response to its environmental drivers. Due to drought, it can be faced a reduction in needle conductance. Light, photosynthesis and stomatal conductance are all related to one another such that a decrease in photosynthesis may be a signal by a hydraulic failure. In fact, the reduction in canopy conductance response may be explained by a decrease in photosynthesis due to sapwood occlusion and hydraulic failure from restricted gas exchange [12]. Sapwood occlusion is a tree response to the spread of pathogens and wood decay organisms, also as part of compartmentalization after wounding. It can be considered to be an effective stress response [8].

Moisture and drought Indexes

	bands	formula
(MSI) Moisture Stress Index	820nm, 1600nm	$\frac{1600}{820}$
(NDMI) Normalized Difference Moisture Index	820nm, 1600nm	$\frac{820-1600}{820+2600}$
(RDI)Ratio drought index	MIR, NIR	$\frac{MIR}{NIR}$

Table 2.4: Moisture and drought indexes' involved spectral bands with their formulas

2.1.3. Tasseled-cap indexes

There are 3 indexes falling into this category:

- Brightness: used to monitor the ground
- Wetness: used to monitor canopy moisture and soil interaction
- Greenness: used to monitor vegetation

They allow computing relevant properties by compressing spectral content in just three indexes through principal component analysis (Table 2.5). Several studies proved that a drop in time of Tasseled cap indexes is related to bark beetle attack, in particular, to identify preliminary stages (green phase) [4] [22].

Tasseled cap Indexes

	bands	formula
Brightness	450:520nm, 520:600nm, 630:690nm, 760:900nm, 1150:1750nm, 2080:2350nm	$0.3037[450:520]+0.2793[520:600]+$ $0.4743[630:690]+0.5585[760:900]+$ $0.5082[1150:1750]+0.1863[2080:2350]$
Greenness	450:520nm, 520:600nm, 630:690nm, 760:900nm, 1550:1750nm, 2080:2350nm	$-0.2848[450:520]-0.2435[520:600]$ $0.5436[630:690]+0.7243[760:900]+$ $0.0840[1550:1750]-0.1800[2080:2350]$
Wetness	450:520nm, 520:600nm, 630:690nm, 760:900nm, 1550:1750nm, 2080:2350nm	$0.1509[450:520]+0.1973[520:600]+$ $0.3279[630:690]+0.3406[760:900]-$ $0.7112[1550:1750]-0.4572[2080:2350]$

Table 2.5: Tasseled cap indexes' involved spectral bands with their formulas

2.1.4. Other indexes

The aforementioned indexes are just a small part of all the possible spectral vegetation indexes that can be computed to analyse the effects of this parasite. All the other indexes not falling into one of the previous categories, are resumed in this section. Foster A. et al (2017) found clear spectral evidence of the correlation between bark beetle attack and Red/Green Index (RGI) [11]. While in [7] the SVM model, trained just with (NGRDI) Normalize Green/Red Difference Index, obtained 63.5% balanced accuracy in the detection of Bark Beetle attack (Table 2.6).

Moisture and drought Indexes

	bands	formula
(RGI) Red/Green index	RED, GREEN	$\frac{RED}{GREEN}$
(NGRDI) Normalize difference Green/red	GREEN, RED	$\frac{GREEN-RED}{GREEN+RED}$

Table 2.6: Other spectral indexes' involved spectral bands with their formulas

2.2. Techniques for Spectral Unmixing in Remote Sensing

Nowadays, hyperspectral satellites have emerged as pivotal scientific tools that, by exploiting their very high spectral resolution, enable the detection of a greater variety of Earth surface materials. However, for technical tradeoff reasons, a denser spectrum sampling must pay the costs of having a lower spatial resolution, as opposed to what usually happens for multispectral satellites, which allow gathering higher spatial resolution images, with coarser spectral resolution. Indeed, a small percentage of radiant energy is accessible in each band, because spectral bands are narrow. As a consequence, the sensor area per pixel must be very wide to achieve an acceptable Signal-to-Noise Ratio (SNR), which causes the geometric resolution to be coarser. In multispectral cameras, the situation is the opposite, a lot of spectral information is left aside since the scene radiance is focused over fewer but wider spectral bands [20]. This project evaluated the feasibility of using PRISMA hyperspectral satellite images to classify trees under bark beetle attack, instead of using field surveys or analyses based on aerial hyperspectral imaging. To this point, PRISMA spatial resolution (30m) could introduce ambiguity in the model, due to the presence of so-called "mixed pixels". Inside a single PRISMA pixel, more than one spectral signature can be hidden, meaning more trees belonging to a different class may be masked by the same larger pixel. For this reason, the benefits of an unmixing procedure will be evaluated. Spectral Unmixing is a diffused technique in the literature and it is often used to create abundance maps or even super-resolution satellite images. These are acquisitions having both high spectral and spatial resolution, which is the result of the combination of hyperspectral and multispectral data.

In this chapter, the aim is to explore various spectral unmixing techniques within the realm of remote sensing. While several methodologies will be presented as examples, it is important to note that this study only focuses on leveraging the Google Earth Engine Unmixing procedure. The decision to utilize this particular approach was driven by the need for enhanced computational power, which was made possible through the utilization of Google's cutting-edge facilities. By employing this powerful tool, we can effectively address the specific objectives of our research with greater efficiency and accuracy.

As for many LSU (Linear Spectral Unmixing) methods, the "ee.Image.unmix()" function in Google Earth Engine (GEE) is used to decompose mixed pixel information into its constituent endmember fractions. This technique assumes that the observed spectral signature of a pixel is a linear combination of the spectral signatures of the endmembers present in that pixel. This function allows to perform spectral unmixing using linear

models and provides the fraction of each endmember present in each pixel of the image. One example of a linear Unmixing procedure is represented by [20], a classical linear spectral mixing model, in which a super-resolution image is computed as a factorization of the acquisition into a non-orthogonal basis of endmembers, also defined as spectral signatures and the related coefficients in this basis, as fractional abundancies, which are a frequency percentage inside the pixel, in the form of maps. In the linear mixing model, the aim is to find the image (Z) by considering the image itself as a linear combination of abundance maps and endmembers, meaning that each pixel “ i ” can be seen as a combination of the spectral signature of a specific material (e_j) and the percentage of material in the pixel for each pixel “ i ” (a_{ij}):

$$z_i = \sum_{j=1}^p e_j a_{ij} \quad , \quad Z = EA \quad (2.1)$$

With a matrix $E = [e_1, e_2, \dots, e_p]$ of pure spectra (endmembers) a matrix $A = [a_1, a_2, \dots, a_{N_m}]$ of per-pixel mixing coefficients (abundances) and $a_i = [a_{i1}; a_{i2}; \dots; a_{ip}]$ the abundances at pixel i . Before computing E and A it is necessary to write H (hyperspectral image) as a spatial downsampled version of the super-resolution one (Z) and the multispectral acquisition (M) as a spectral downsampled version of Z . Therefore, H can be written as:

$$H \approx ZBS = EABS = E\tilde{A} \quad (2.2)$$

Where B is a matrix that blurs A accordingly to the hyperspectral sensor’s spatial response and S , also known as downsampling operator, depends on the difference in resolution between the two acquisitions. Therefore, $\tilde{A} = ABS$ can be considered as lower resolution abundances and considering that all the hyperspectral bands are blurred in the same way, it results that the effect is the same as blurring A directly. The multispectral image M , instead can be written as:

$$M \approx RZ = REA = \tilde{E}A \quad (2.3)$$

Where $\tilde{E} = RE$ are the spectrally reduced endmembers and R the sensor’s spectral response. B and R , respectively the hyperspectral spatial response function and the multispectral spectral response function, are either given by camera specifications, or they can be computed by combining equation (2.2) and (2.3):

$$MBS = RH \quad (2.4)$$

Finally, starting from the following constraints:

$$a_{ij} \geq 0 \quad \forall i, j \quad (2.5a)$$

$$\mathbf{1}^T A = \mathbf{1}^T \quad (2.5b)$$

$$0 \leq e_{ij} \leq 1 \quad \forall i, j \quad (2.5c)$$

Where constraint (2.5a) stands for non-negative abundance, constraint (2.5b) for abundances sum to one and (2.5c) for non-negative, bounded reflectance. In addition, taking into account the aforementioned equation (2.2), (2.3), (2.5a), (2.5b) and (2.5c), the problem can be solved by computing endmembers and abundancy maps (E and A) from a least square minimization procedure:

$$\min_{E,A} \frac{1}{2} \|H - EABS\|_F^2 + \frac{1}{2} \|M - REA\|_F^2 + \frac{\lambda}{2} \|AD_h W\|_F^2 + \frac{\lambda}{2} \|AD_v W\|_F^2 \quad (2.6)$$

Where equation (2.6) is subject to constraints (2.5a), (2.5b), (2.5c) and $\|A\|_0 \leq s$. Where $\|\cdot\|_F$ stands for the Frobenius norm and $\|A\|_0$ is the number of non-zero elements of A. D_h and D_v are, instead, the matrices computing the discrete gradients between neighbouring pixels in the horizontal and vertical directions. W is a diagonal weight matrix and λ has control over the strength of the regularization [20]. Code for Lanaras' CMF (Coupled Matrix Factorization) is freely available on GitHub at [Lanaras code Matlab](#).

In [32] other three unmixing algorithms are explained as possible solutions to mixed pixels issues, in particular CNMF (Coupled Nonnegative Matrix Factorization), Akhtar's Method and HySure. As for Lanaras' CMF [20], CNMF [31] computes super-resolution images as the product of the spectral signatures and the high-resolution abundance maps. The difference with respect to [20] is that CNMF initializes its spectral endmembers by VCA [24] (Vertex Component Analysis) as opposed to SISAL [5] (Split Augmented Lagrangian) for Lanaras and later CNMF alternately unmixes the HS and MS images by NMF [21] (Normalized Matrix factorization) to estimate the spectral signatures, instead of using a projected gradient method. Python and Matlab code can be downloaded from the Naoto Yokoya web page, at the following link: [CNMF code](#). Akhtar's algorithm, instead, uses an online dictionary-learning method to obtain the spectral signatures of the endmembers. On the other side, high-resolution abundances are computed from sparse coding ([Akhtar's method code](#)) Hysure is another different algorithm which uses variation regularization into the subspace-based Hyperspectral–Multispectral fusion framework, which is computed as the minimization of a convex objective function in relation to subspace coefficients. Then, the subspace transformation is obtained by endmember extraction or by SVD (of the low-resolution Hyperspectral image). The full code implementation can

be accessed at [HySure code](#). Among these four algorithms, Yokoya et al. (2017) identified HySure as the best in terms of performance, immediately followed by CNMF; Akhtar's lies in the last position, while Lanaras performs slightly better (with respect to Lanaras only). Finally Hong et al. (2022) [16], recently proposed a new solution, inspired by Deep Learning techniques. Differently from all the previously mentioned methods, this algorithm allows to achieve higher performances, disregarding sensor-related information, needed for sensor calibration. This type of information is, indeed, often hard to be gathered, hence this is a great advantage for unmixing purposes. The purpose is to model a novel network architecture (DC-Net), consisting of two subnetworks. First, DC-Net decomposes Hyperspectral and Multispectral data in order to get common content and sensor-specific information, then the latter is used for a better fusion between HS and MS data. Finally, this sub-pixel fusion is computed by taking as input the recombined HS-MS image and producing as output the classical abundancies and endmembers. As stated by Hong et al. (2022) "DC-Net behaves superiorly compared to ex-using state-of-the-art DL approaches," but also outperforms Lanaras algorithm in 5 picture quality indexes out of 5. Although all these implementations are often used unmixing procedures, the spatial distribution of each endmember in the mixed pixel often still remains unknown. This project, in particular, aims not only at implementing an unmixing procedure, by exploiting the high resolution of a hyperspectral airborne sensor (rather than multispectral, as commonly done in literature [20]), but also to track down the spatial distribution of the different abundance percentages, thanks to a subpixel mapping with respect of the 30m resolution pixel of PRISMA. By subdividing the "mixed pixel" into smaller and more "subpixels" and by assigning to each pixel a specific class, this technique will allow classifying at higher resolution starting from lower resolution abundance maps [29]. The whole principle is based on spatial dependence, which refers to the tendency for spatially close observations to be more alike than distant observations. To this purpose in [23] Sub-pixel mapping (or super-resolution mapping) was formally introduced by Atkinson. To implement the Atkinson algorithm it is necessary, first of all, to define a scaling factor S , where S^2 represents the number of high-resolution subpixels (aerial hyperspectral sensor) contained in the low-resolution image (PRISMA). In addition to this, it should be previously defined the neighbourhood model, namely which pixels will be considered as neighbours and, thus, the only ones that will be used to assign a class to the selected subpixel.

The choice is restricted to one of the following 3 models:

- Touching neighbourhood: Only pixels physically touching the sub-pixel under consideration

- Quadrant neighbourhood: Only pixels in the same quadrant as the sub-pixel with respect to the centre of its comprising pixel
- Surrounding neighbourhood: All surrounding pixels

A visual representation of the aforementioned neighbourhood models is shown in Figure 2.1.

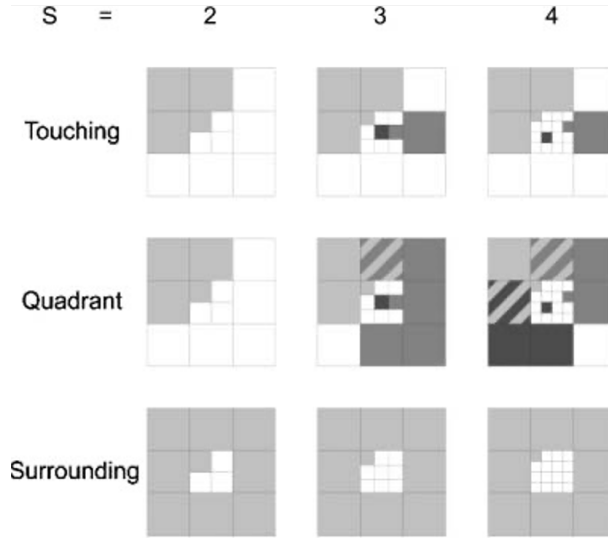


Figure 2.1: Visual representation of the three neighbourhood models as a function of the scale factor S . Credits: [23].

The raw attraction value $p_{a,b}(c)$ for sub-pixel $p_{a,b}$ is calculated as the average of all fraction values $P_{i,j}(c)$ of the pixels $P_{i,j}$ in the neighbourhood of $p_{a,b}$ divided by the distance between pixel $P_{i,j}$ and sub-pixel $p_{a,b}$:

$$P_{a,b}(c) = Avg \left\{ \frac{P_{i,j}(c)}{d(P_{a,b}, P_{i,j})} \mid P_{i,j} \in N_t[P_{a,b}] \right\} \quad (2.7)$$

It is important to underline that in $P_{i,j}$, “i” and “j” are referred to the coordinates of the top left subpixel in the high-resolution image, used to identify the bigger low-resolution neighbour pixel $P_{i,j}$. Furthermore, the distance between the neighbour pixel and the subpixel is computed as:

$$d(P_{a,b}, P_{i,j}) = \sqrt{[a + 0.5 - S(i + 0.5)]^2 + [b + 0.5 - S(j + 0.5)]^2} \quad (2.8)$$

Finally, in Equation (2.7), $N_t[P_{a,b}]$ identifies one of the three aforementioned neighbourhood models, whose equation can be found in (2), (3) and (4) of [23]. Once the attraction value $p_{a,b}(c)$ is computed for each subpixel in each category, this value will explain the

amount of attraction of the subpixel $p_{a,b}$ to the class c . Therefore, these values can then be used for the assignment of sub-pixels to the different classes: sub-pixels with the highest attractions are assigned first.

Different studies also evaluated the possibility to consider spatial correlation among the different image's pixels [30], [9], [3]. Moreover, this is a possible solution that can improve the abundance classification of the single pixel and consequentially the pixel's classification quality.

3 | Material and Methods

3.1. Sensors and Data

As anticipated, the hyperspectral satellite chosen to replicate and possibly improve Beetle's detection performed by the aerial asiaFENIX sensor is PRISMA (launched by ASI - Agenzia Spaziale Italiana on 22th of March 2019). The main characteristics of the two sensors have been reported in the following list:

- **AisaFENIX**: Hyperspectral aerial data has been gathered by the AisaFENIX sensor, from Specim company. This sensor acquires data in push broom modality, with a spectral resolution of 345 bands and a spatial resolution of 2m, distributed in a continuous spectral span (which ranges between 400nm – 2500nm). These specifics allow for good spectral compatibility with PRISMA. The aerial data extracted from the initial survey has the following structure:
 - Datacube: band sequential data file, it contains all the intensity values atmospherically corrected by the ACTOR4 software, to be converted to reflectance during the pre-processing phase.
 - Classification Map: Raster file, this map has been pre-computed and provided by the "AVT AS" company to be used as "ground truth" because of the absence of field survey data. It provides a classification of the area by assigning one of the 7 categories to each pixel: 0 for "unclassified", 1 for "dead spruce", 2 for "spruce", 3 for "larch", 4 for "deciduous trees", 5 for "shadow" and 6 for "scotch pine" (Figure 3.1 and 3.2). These maps have been computed from the analysis of the following indexes: Anthocyanin Reflectance Index, Atmospherically Resistant Vegetation Index, Carotenoid Reflectance Index, Carotenoid Reflectance Index, Enhanced Vegetation Index, Leaf Chlorophyll Index, Modified Chlorophyll Absorption Ratio Index, Modified Red Edge Normalized Difference Vegetation Index, Modified Red Edge Simple Ratio, Modified Triangular Vegetation Index, Normalized Difference Vegetation Index, Optimized Soil Adjusted Vegetation Index, Photochemical Reflectance Index,

Plant Senescence Reflectance Index, Red Edge Normalized Difference Vegetation Index, Red Edge Position Index, Red Green Ratio Index, Simple Ratio, Structure Insensitive Pigment Index, Sum Green Index, Transformed Chlorophyll Absorption Reflectance Index, Triangular Vegetation Index, Vogelmann Red Edge Index.

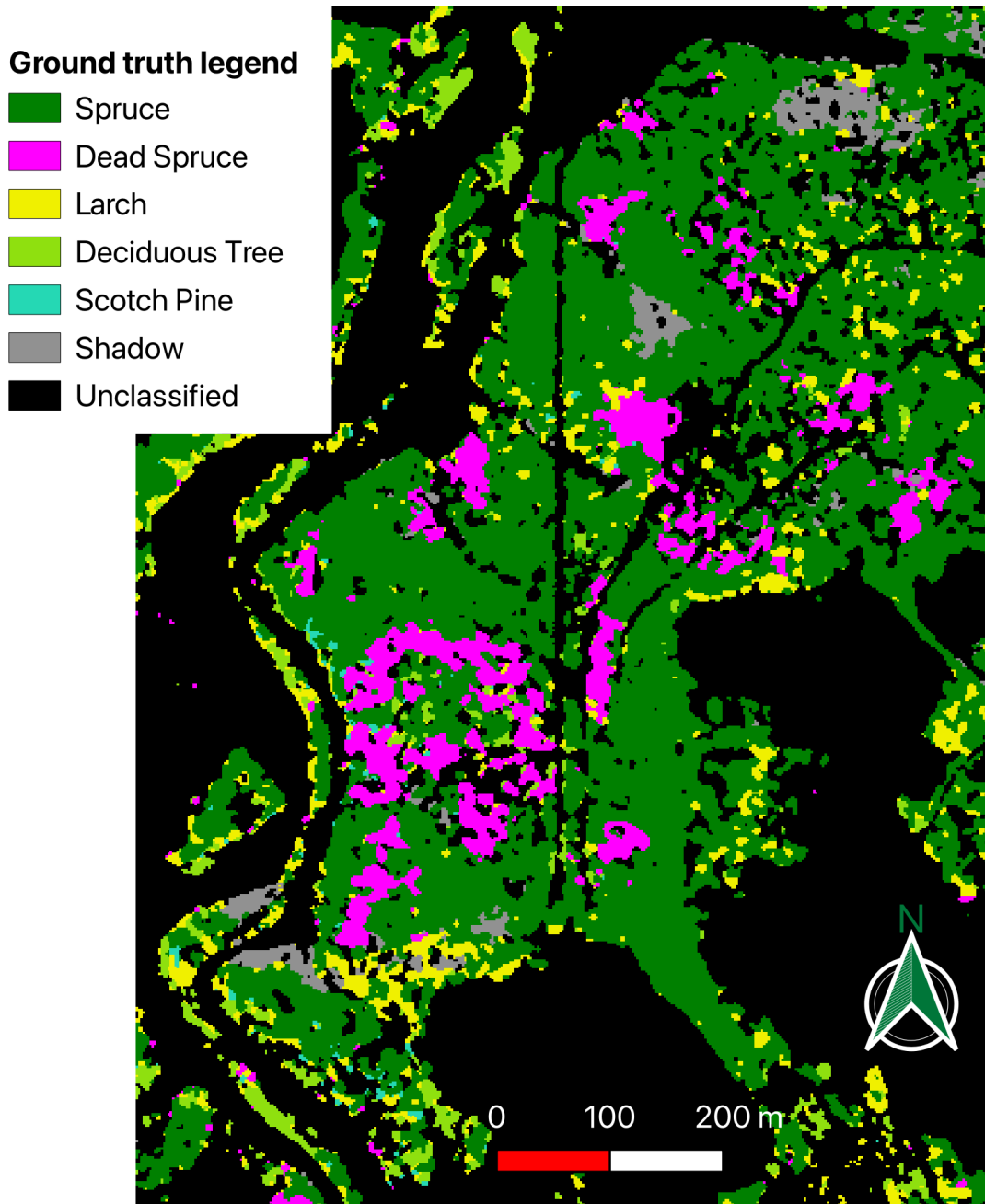


Figure 3.1: Area 5 classification map provided by the AVT AS company

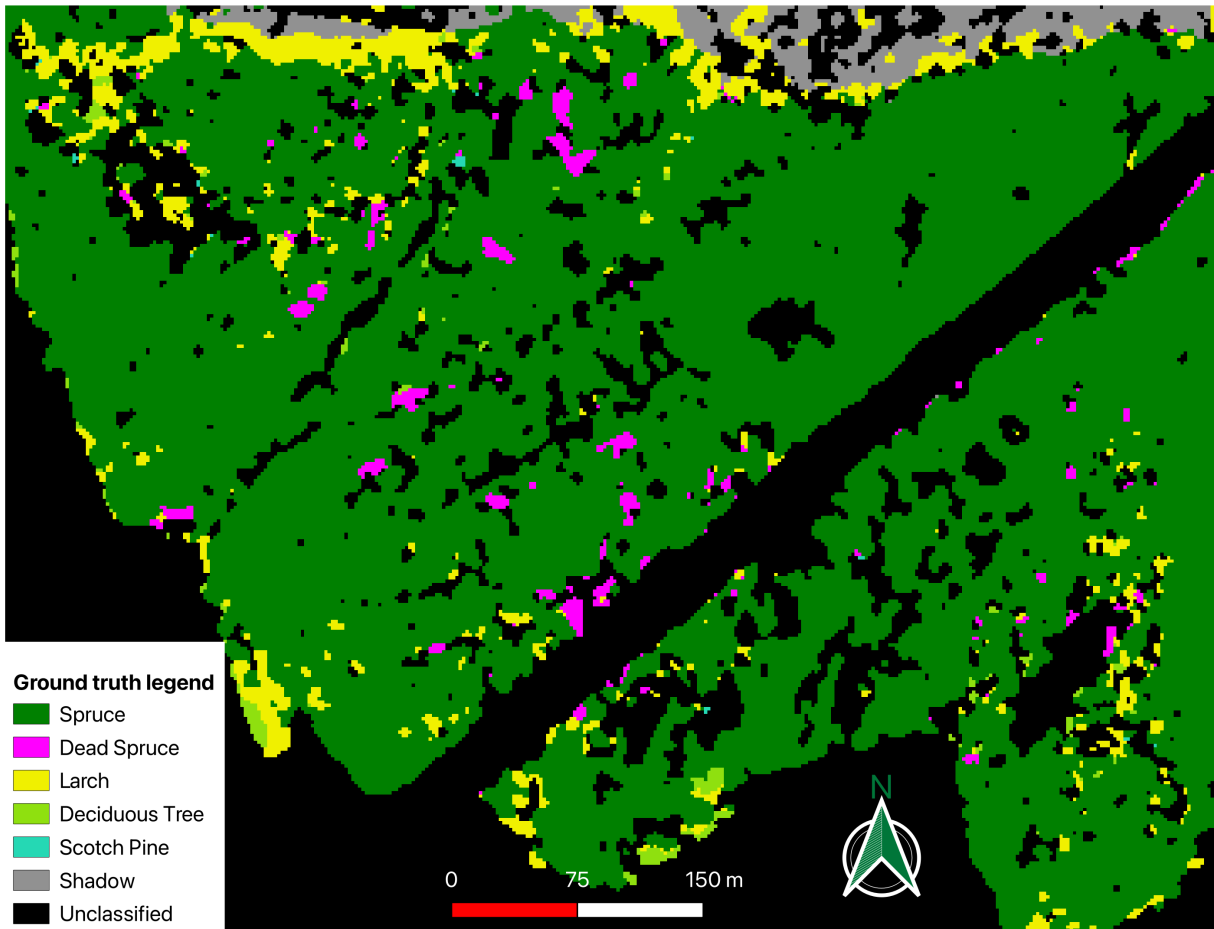


Figure 3.2: Area 3 classification map provided by the AVT AS company

- **PRISMA:** it is a Sun-synchronous hyperspectral satellite, deployed by ASI (Agenzia Spaziale Italiana). Its revisit time is 29 days with a relook of 7 days and it is a pushbroom satellite based on a prism technology. Being a hyperspectral satellite, PRISMA can cover the 400– 2500 nm spectral range with 240 bands (split in 66 bands for the Visible and Near Infrared cube and 174 for the Short Wave Infrared one) at a very small spectral resolution (9–13 nm VNIR and 9–14.5 nm for SWIR). Acquisitions are taken with a swath of 30km at a spatial resolution of 30.7m [6]. PRISMA has also an additional band, coming from a panchromatic sensor, with a higher GSD (5m), that can be used to improve the spatial resolution with the help of pansharpening techniques [18] (those methods have not been used in this study).

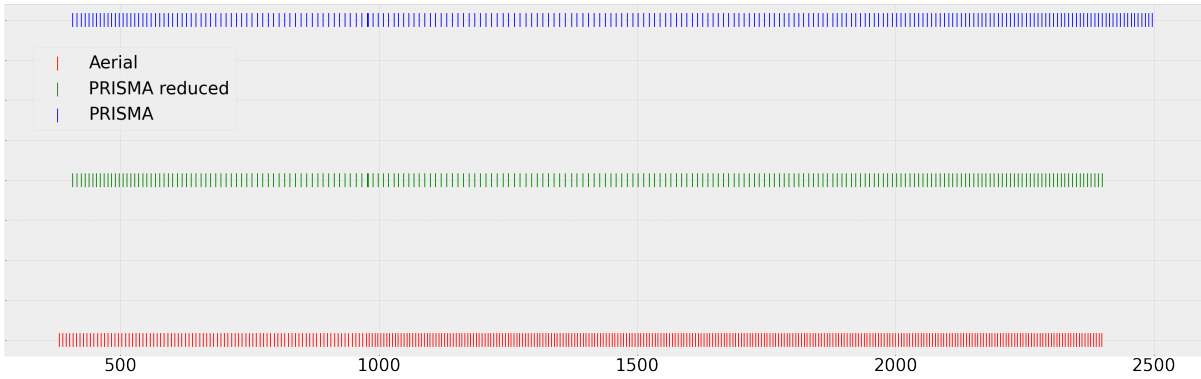


Figure 3.3: A visual representation of PRISMA and AisaFENIX" bandset; each segment represents a sensor band (wavelengths in nanometers) for the Aerial, PRISMA and PRISMA reduced hyperspectral cube (the latter is a PRISMA cube with a cut on the last 15 bands, to match the same final wavelength of the aerial sensor, as it will be further explained in the next chapters)

In order to have a proper validation (with the aerial data) of the PRISMA analysis that has been developed, it is important to have temporal coherence between the aerial sensor acquisition and the satellite one.

Since the aerial survey has been performed on 8th of October 2022, the closest cloud-free acquisition in time, intersecting the Gadertal area, has been researched in the PRISMA catalogue through the ASI portal.

As a result, the best match in the PRISMA catalogue has been found on October 16th 2022. In the following table, the main information on the aerial and PRISMA acquisitions has been resumed:

	Date	Central Coordinates (lat,long)
PRISMA	16/10/2022	46.565, 11.771
aerial	08/10/2022	43.626,11.895

Table 3.1: Satellite and aerial image information

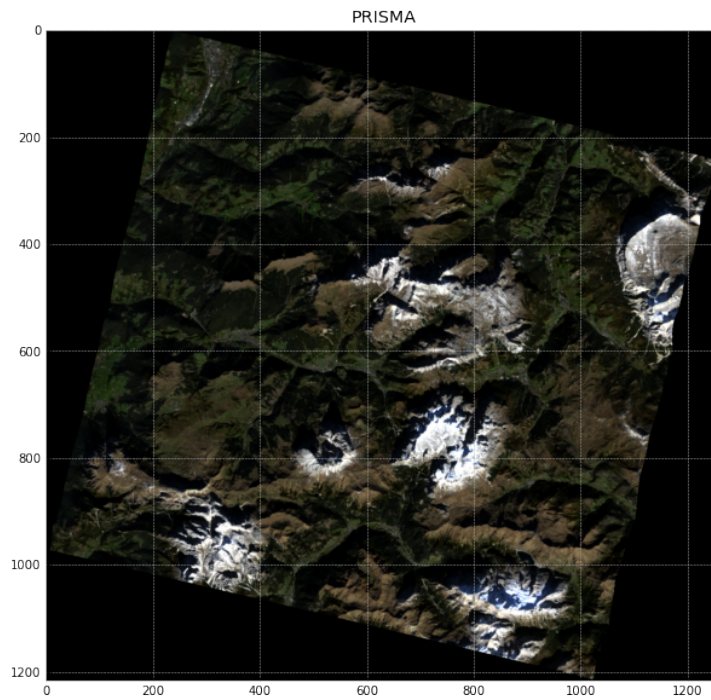


Figure 3.4: RGB representation of PRISMA's study area. The pixel coordinates are represented on the x and y axis (as for all the other following images)

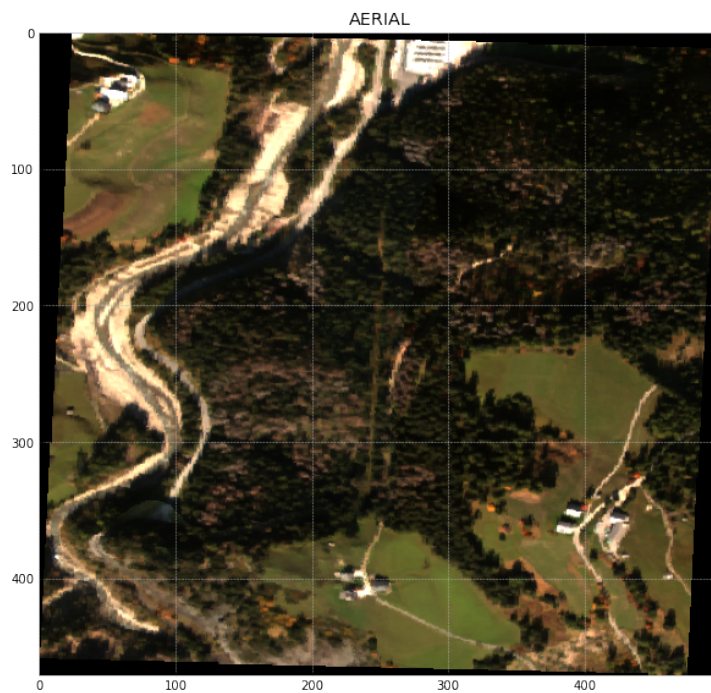


Figure 3.5: RGB representation of aerial study area (area 5)

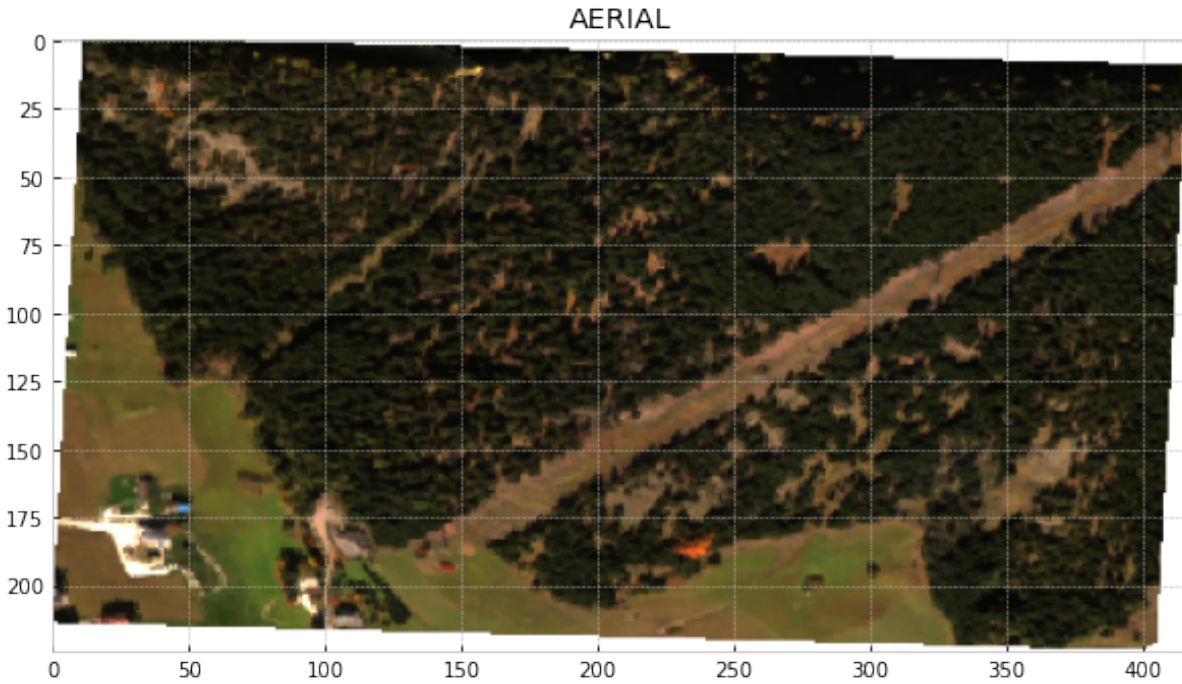


Figure 3.6: RGB representation of aerial study area (area 3)

The full code implementation of this study can be freely accessed on [GitHub](#). In developing the Python code for this project, the power of several libraries and technologies has been exploited. Key among these were numpy, rasterio, gdal, h5py, PIL, cv2, scipy, sklearn, seaborn, pandas, and geopandas. The numpy library enabled efficient numerical operations and array manipulation, while rasterio and gdal facilitated the handling and processing of geospatial raster data. h5py provided a convenient interface for working with the Hierarchical Data Format (HDF) in which PRISMA data is provided, and PIL empowered image processing capabilities. Additionally, cv2 (OpenCV) was used to aid image interpolation and resizing tasks, while scipy facilitated scientific statistical test computations (e.g. Shapiro test). To produce validation matrices, sklearn (Scikit-learn) offered a comprehensive toolkit, and seaborn provided aesthetically pleasing visualizations. Finally, the combined power of pandas and geopandas allowed for efficient data manipulation and analysis, particularly for geospatial datasets. Leveraging these libraries and technologies greatly enhanced the efficiency and effectiveness of the project.

3.2. Pre-Processing

Pre-processing is a crucial step in remote sensing data analysis. In this preliminary phase, images are prepared to go through the main processing of the study: the Beetle detection.

As anticipated from Figure 3.8, the procedure has been customized accordingly to the type of sensor: aerial or satellite. In figure 3.7 a legend of the chapter flowchart is presented.

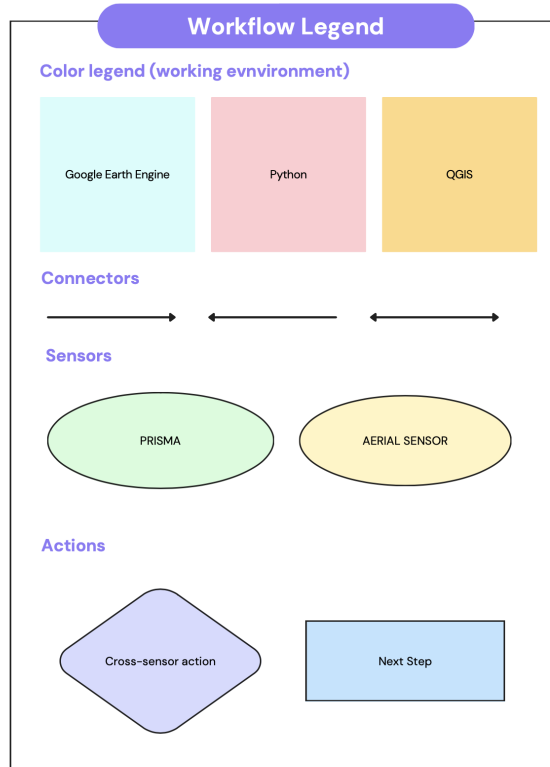


Figure 3.7: legend workflow schema

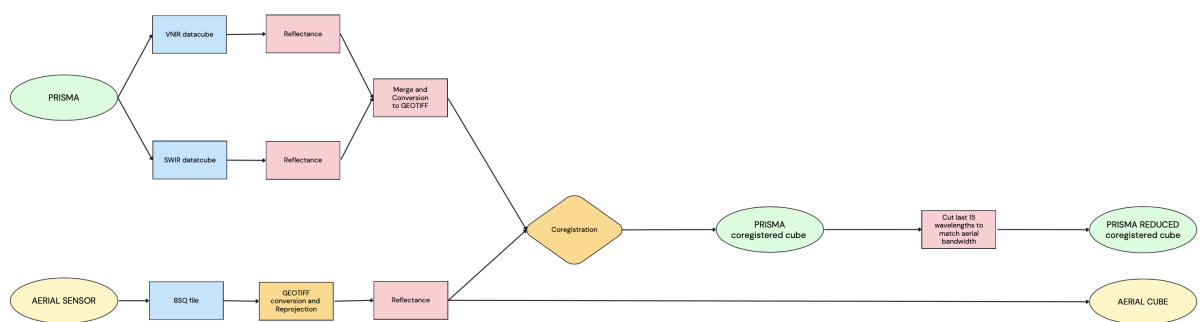


Figure 3.8: pre-processing workflow schema

3.2.1. PRISMA data pre-processing

After downloading the acquisitions from the PRISMA portal at their highest available processing level (L2D), the data have been first accessed in the HDF5 (Hierarchical Data

Format) format and then copied inside two different data cubes (a Numpy stack of the different bands stacked along the third dimension, one for VNIR and another for SWIR) and then processed in order to transform the raw Digital Number into a reflectance value, following the procedure explained in PRISMA manual ([User Manual](#)).

$$XXX = L2scaleXXX_{min} + XXX_{DN} \frac{(L2scaleXXX_{max} - L2scaleXXX_{min})}{65.535} \quad (3.1)$$

Where XXX refers to the specific datacube of the dataset: “PAN”, “VNIR” or “SWIR”. Finally, the VNIR and SWIR cubes (in WGS84 Coordinate Reference System) have been stacked together, converted into a TIFF file and projected to UTM zone 32N to be compatible with aerial data. The separation of the two datacubes before computing the reflectance is crucial since the scaling factor in equation 3.1 is specific for the type of cube (different from VNIR to SWIR).

After those initial steps, the first output of the procedure is created: the reflectance PRISMA datacube.

The TIFF file obtained, however, is not perfectly aligned with the aerial data. This phenomenon suggests the need for a coregistration step.

Coregistration is a fundamental task in remote sensing data analysis because it allows images to be perfectly overlapped and match each other. The classification analysis can benefit from coregistration, by reducing the number of ‘false positives’ or ‘false negatives’ (wrongly detected because of the misalignment of the aerial and satellite acquisition). According to [28], PRISMA L2D data is already geocoded and orthorectified, but the lack of PRISMA Ground Control Points, causes the georeferencing accuracy to reach a very low level, where images from the same sensor in different time instants are shifted in the order of 2-3 pixels (up to 5-8 pixels).

Since the two sensors have different ground coverage, it would have been complicated to rely on coregistration techniques based on pixel intensity (e.g. Gefolki [26]), because images need to have the same extent and frame the same portion of land. By cropping the PRISMA acquisition to the small local area framed by the asiaFENIX aircraft sensor of 758m x 1064m, it would only be possible to coregister satellite data in this zone and not to its complete 30km x 30km extent.

Given that, it has been chosen to not perform a proper coregistration, but an actual new georeferencing for the satellite image. By doing so, the aerial image is taken as a reference, so that PRISMA and asiaFENIX data could share the same GCP grid (actually the aerial GCP grid, since as anticipated is the most accurate between the two).

Since the procedure is only necessary in order to avoid errors in the validation step, the satellite image has been coregistered only with area 3 of the aerial sensor, which is the

hold-out data, used for the validation step. The procedure has been implemented on QGIS, by manually selecting a set of double points (points corresponding to the same pixel on both aerial and satellite data) as evenly distributed on the image border and centre as possible (given the lack of recognizable features, due to the low resolution of PRISMA images). In order to explore the best possible algorithm for the transformation, a k-fold cross-validation technique has been implemented, comparing the residuals of each procedure:

- Linear transformation
- Helmert transformation
- 1st degree Polynomial transformation
- 2nd degree Polynomial transformation
- Projective transformation

In the k-fold validation procedure, the first set of fixed points has been chosen (used for warping), meaning that none of those points will be removed in each step of the k-fold comparison. The smallest set of remaining points has been kept as leave-one-out so that the residuals will be computed for each transformation as many times as the leave-one-out points (k). The residuals evaluated leaving out each point of the smallest set, will be later averaged, in order to assign a mean residual pixel value to the transformation type. Finally, after comparing the different residuals and once the transformation has been chosen, the reflectance cube is georeferenced on the aerial data and a new coregistered cube is produced as output.

The second output of the pre-processing phase is obtained by cutting out the last 15 bands from the datacube, resulting in a new "reduced" datacube of 215 bands. This intermediate result is fundamental for the following "band pairing" procedure, in the Unmixing step. Here, each band of the aerial sensor (345 in total) is paired to the closest band of the PRISMA reduced cube (215 in total). Without this removal, the band pairing algorithm wouldn't perform correctly, whereas by removing the last 15 satellite bands, the last wavelength in the cube would be the same as the aerial one (2400nm as explained in Figure 3.3, instead of 2500nm for the original PRISMA image). For a deeper explanation of the band-pairing algorithm see Section 3.3.

In the following list, the inputs and final outputs of the PRISMA pre-processing step have been summarized:

INPUTS:

- PRISMA cube: datacube, composed of raw DN (digital numbers) of the PRISMA

acquisition

OUTPUTS

- PRISMA coregistered reflectance cube: datacube, composed by reflectance values and aligned with the aerial acquisition
- PRISMA reduced cube: coregistered reflectance cube, which size is reduced from 230 bands to 215 (cut on last 15 wavelengths)

3.2.2. asiaFENIX data pre-processing

The asiaFENIX acquisitions are provided in a BSQ (band sequential) data format, which is projected in "WGS84 / UTM zone 32N".

Since the images have been already preprocessed by the AVT AS company, the procedure to convert raw values into reflectance is not as complex as the satellite one. Therefore, after the atmospheric correction of the ATCOR4 software used by the company, the data is delivered with a reflectance scale factor of 10000 and a "No Data" value of 15000, so the procedure used to correct the values is the following:

$$reflectance = \frac{DN}{10000} \quad (3.2)$$

Where DN stands for Digital Number. Once the reflectance is computed, Area 3 of the aerial study area is used as a reference to coregister PRISMA images (as explained in Section 3.2.1).

In the following paragraph, the inputs and final outputs of the asiaFENIX pre-processing step have been summarized:

INPUTS:

- Aerial BSQ file: datacube, composed by raw DN (digital numbers) of the asiaFENIX acquisition

OUTPUTS

- Aerial reflectance cube: GeoTIFF datacube, composed by reflectance values of the asiaFENIX acquisition

3.3. Spectral Unmixing

Since the difference in spatial resolution of the aerial and satellite sensor is very significant, the analysis may suffer from the presence of the so-called "mixed pixels". As anticipated,

the PRISMA sensor has a resolution of almost 30.7m, while asiaFENIX allows for a resolution of 2m, this means that a single satellite pixel may contain approximately 240 aerial pixels. Given that, it is clear that different classes of land cover (unclassified, dead spruce, spruce, larch, deciduous trees, shadow, scotch pine) may be contained in the same PRISMA pixel. The strategy adopted to estimate the percentage of pure PRISMA pixels is to compare the satellite acquisition with the classification map of the company, which allowed the computation of the percentage of pixels containing a unique class.

From this analysis, it turned out that only the 25% of PRISMA pixels (intersecting with area 5) are pure and the 99% of these pixels fall in the category of unclassified pixels, while just the remaining 1% are pure Spruce tree pixels. This undoubtedly explains why it is crucial to apply Unmixing (the general schema followed in this study is presented in Figure 3.9).

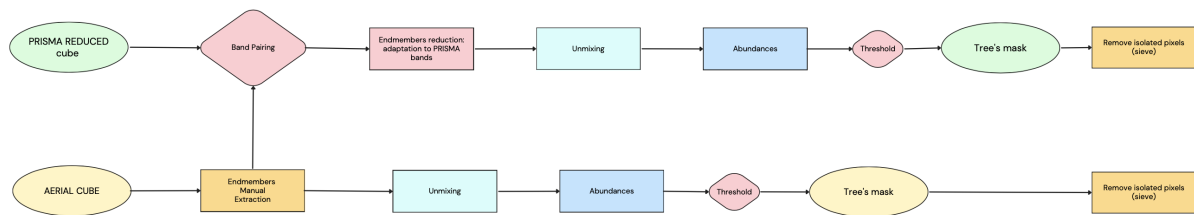


Figure 3.9: unmixing workflow schema

Since the unmixing algorithms require large computational capabilities, Google Earth Engine has been chosen as an auxiliary platform for the implementation. By simply making use of the "ee.Image.Unmix" ([GEE Unmix](#)) procedure (see section 2.2), this powerful function is able to produce several abundance maps of different user selected classes, exploiting Google resources to speed up the computation.

Given that the main objective of this study is to inspect spectral indexes of trees only, to detect the ones affected by possible diseases, it is necessary to detect trees' crowns first. In this way, the index extraction can be isolated just in the area covered by trees.

That being said, the unmixing procedure has been adopted with the main goal of creating trees' binary masks. Before producing the abundance map, the user is required to select the different classes that need to be detected by the algorithm, and in particular, given the features contained in the studied acquisitions, it has been chosen to inspect the following categories:

- **Healthy trees:** areas of green and healthy trees
- **Unhealthy trees:** tree's areas affected by visible diseases (grey/red leaves)

- **Unvegetated areas:** area not covered by green vegetation (artificial surfaces, bare soil, snow and river bed)
- **Grassland:** areas covered by green grass
- **Water:** rivers or lakes
- **Shadow:** pixels in which the shadow, produced by trees' canopy, buildings, hills and many other features, obstruct the classification

3.3.1. AsiaFENIX image spectral unmixing

The first step of the unmixing procedure is the extraction of the endmembers, also known as spectral signatures as shown in Figure 3.9. Each different surface type, such as grassland, water, trees, and shadows reflects radiation in each channel in a peculiar way. The spectral signature is the radiation reflected as a function of the wavelength. Since the aerial sensor contains 345 bands, while the PRISMA one has only 230, the aerial cube has been used as a reference to extract the spectral signature, in order to exploit the content of the sensor with greater spectral resolution.

Spectral signatures have been extracted from QGIS, by manually defining vector regions of interest (ROI), for each unmixing class. Once ROIs have been chosen, it has been selected the median of the reflectance of each pixel inside every region for each band of the sensor, which produced a set of 6 arrays with size 345 (one reflectance value for each band of the sensor). As already stated, the operator used to average the pixel values in each region is the median, which is a more robust indicator of the actual average reflectance in case outliers are present (differently from the mean operator).

ROIs have been created starting from area 5 and inferring classes from the RGB representation, as can be observed in Figure 3.10.

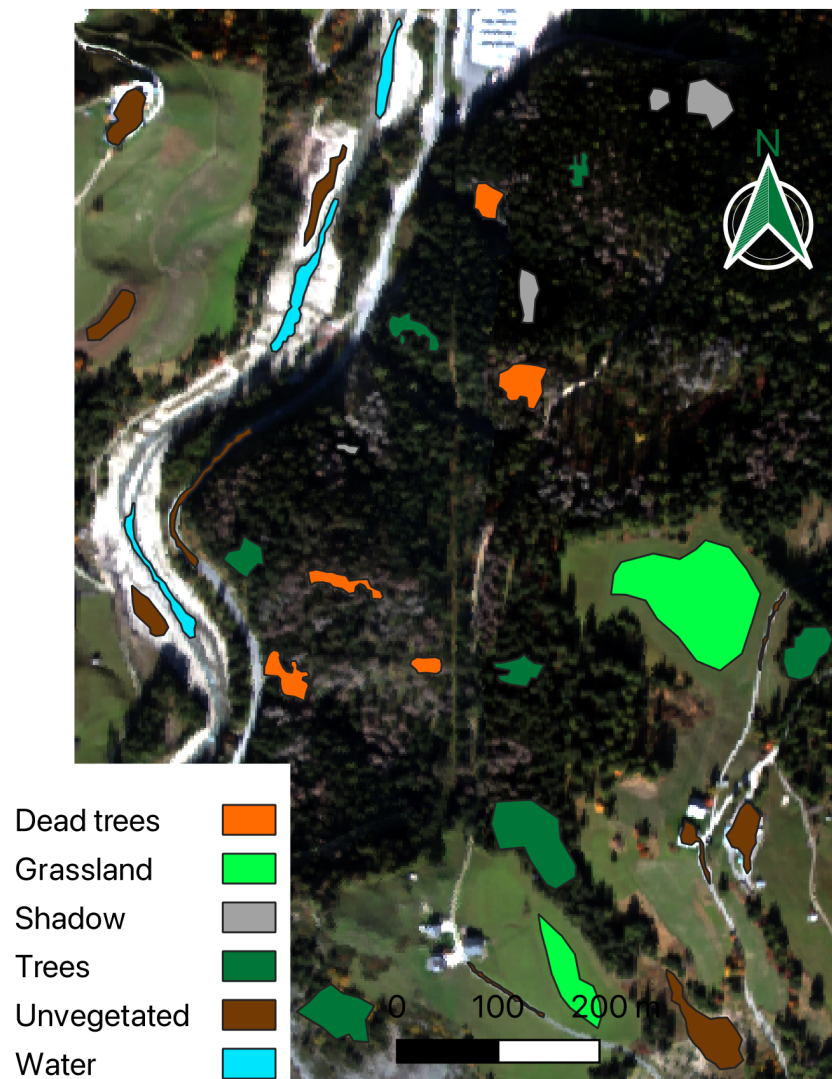


Figure 3.10: Training regions of interest for the unmixing procedure

Aerial endmembers' spectral signatures are used as input of the Google Earth Engine "ee.Image.Unmix" procedure, together with the aerial cube, and the function will return the abundance maps of each selected class. Abundance maps are in the form of TIFF files, as single bands containing a percentage value. Each value represents the raster of a given class contained in each pixel, expressed as the percentage of mixing. By summing up all values belonging to the same pixel in each abundance map, the result obtained would be 1 (100%).

Since abundance maps contain continuous values ranging between 0 and 1, it is not possible to use them as masks to filter out trees' crowns. To overcome this, a threshold has been selected to produce binary maps from trees' abundance maps. Binary maps are produced just for two classes, which are healthy and unhealthy trees, which will be unified

(by a simple union operation) to obtain a single binary mask for trees. The threshold to extract binary images is calibrated on the area 5 classification, provided by the company. The percentage of healthy and unhealthy pixels is deduced by counting pixels belonging to these classes in the classification map. The percentage ($Pixel\%$) is not directly applied to filter the abundance map, but it will be used to define the percentile. This percentile is the abundance value that will split the continuous distribution into two separate groups (Percentile = $100\% - Pixel\%$): the values greater than the percentile will be considered as ones while the lower ones as zeros. In this way, only the $Pixel\%$ of the highest values in the image (the most representative of that class) will be extracted, therefore the binary map will reflect the same percentage of healthy and unhealthy trees estimated by the company.

The abundance value of pixels extracted with the aforementioned technique may include also low abundance percentages, which are not exactly representative of the class they are assigned to. Nevertheless, the low spatial resolution of PRISMA increases the number of mixed pixels in the image, reducing considerably the number of pure pixels, which makes the selection of a more conservative threshold a needed choice.

Since binary maps produced in the aforementioned way, are affected by the so-called "salt and pepper" effect, they will go through an additional processing step before being used: sieving. In order to remove the isolated pixels and smooth the results, a median blur filter is applied to the binary image, with the following formula. This is a non-linear filtering technique, that takes a median of all the pixels under the kernel area and replaces the central element with this median value. That technique is quite effective in reducing a certain type of noise (including the salt-and-pepper one) with considerably less edge blurring as compared to other linear filters of the same size.

Once produced, the final binary tree binary mask will be useful in the next step of Spectral Indexes Extraction (Chapter 3.4).

INPUTS

- Aerial reflectance cube: output of the previous pre-processing step

OUTPUTS

- Endmembers arrays: 6 arrays of size 345, containing a reflectance value for each band of the aerial sensor. Each array is the pure signature of the six unmixing classes
- asiaFENIX trees' masks (one for healthy and one for unhealthy trees): binary mask of tree's canopies (1 for tree's pixels, and 0 for non-trees)

3.3.2. PRISMA image spectral unmixing

After endmembers are extracted from the aerial sensor, they need to be transformed in order to be used with the PRISMA datacube for the same unmixing procedure. As anticipated in the previous section, this will allow augmenting the satellite's spectral capabilities by leveraging the aerial high spectral resolution data. Therefore aerial endmembers need to be resized, from a vector of length 345 to a vector of size 230, so that it will match the PRISMA satellite band number.

To reach this objective, a technique to pair the different bands of the aerial and satellite sensor was implemented by averaging aerial bands in groups. First of all, each PRISMA band (wavelength) is associated with an id (1,2,3...230). Then, each aerial wavelength is assigned with the id of the corresponding closest PRISMA band, creating what has been named as "pairing array" (Figure 3.11).

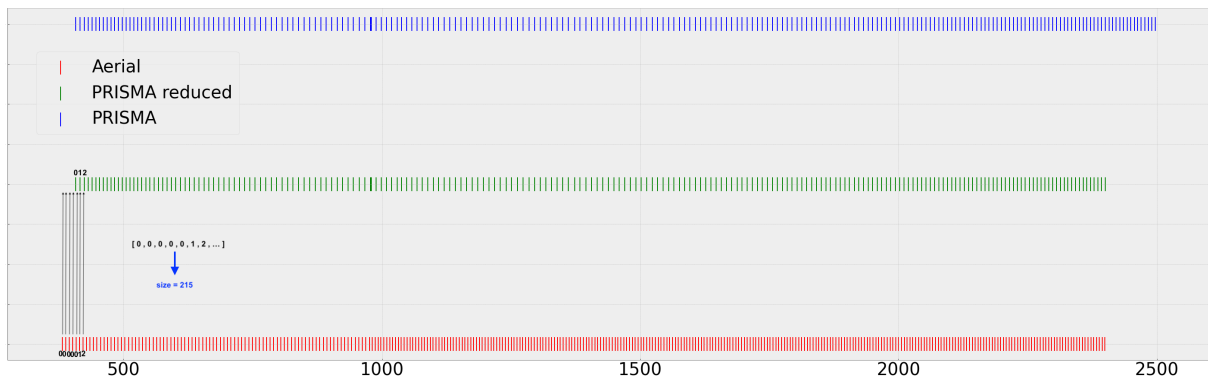


Figure 3.11: Visual representation of the "pairing array" extraction

Once obtained, the "pairing array" is used to average the aerial endmembers, by computing the mean of all the aerial endmembers with the same id and finally obtaining an endmember vector of 230 bands, suitable for satellite data.

In order to validate this approach, spectral signatures of the 9 pure tree PRISMA pixels have been compared with the 1924 aerial ones, falling inside this first 9.

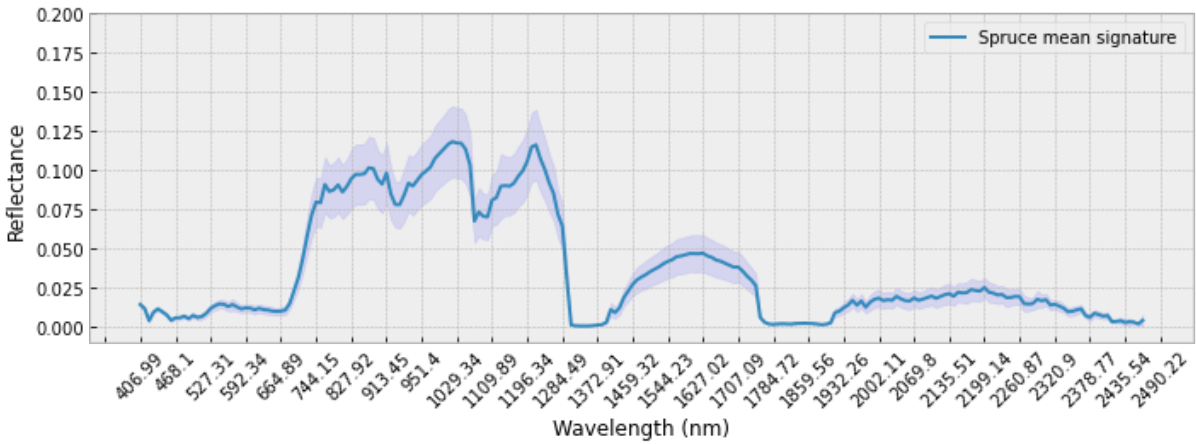


Figure 3.12: Mean and standard deviation of pure PRISMA healthy Spruce trees' spectral signatures. The solid lines represent the mean of the 9 spectral signatures of PRISMA and the 1924 ones of asiaFENIX, while the transparent area around it, identifies the standard deviation of the same endmembers

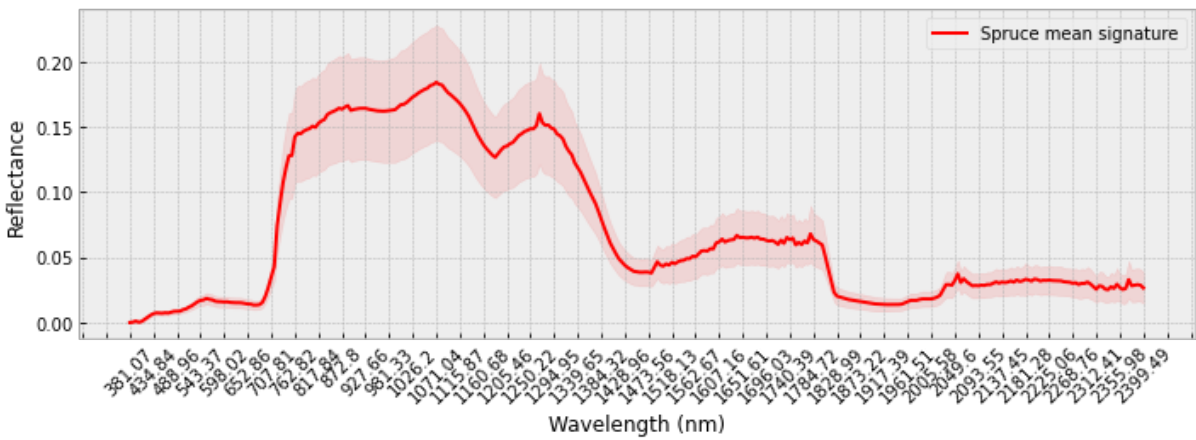


Figure 3.13: Mean and standard deviation of pure asiaFENIX healthy Spruce trees' spectral signatures. The solid lines represent the mean of the 9 spectral signatures of PRISMA and the 1924 ones of asiaFENIX, while the transparent area around it, identifies the standard deviation of the same endmembers

Figure 3.12 and 3.13, show respectively the mean and standard deviation of the reflectance value assumed in the different wavelength spans.

As can be appreciated from this comparison, the two spectral signatures have the same trend over almost the same spectral range, with a small difference in the reflectance peak reached in the curve between 600nm and 1300nm (0.2 for asiaFENIX and 0.125 for

PRISMA).

This spectral correspondence, reveals a good compatibility of cross-sensor signatures, which enforces the validity of the band pairing procedure.

Finally, once satellite endmembers are computed, the trees' binary masks are extracted in the complete PRISMA tile with the same pipeline explained for the aerial sensor in Section 3.3.1.

INPUTS

- PRISMA reduced cube: output of the pre-processing step
- Endmembers arrays: 6 arrays of size 230, containing a reflectance value for each band of the satellite sensor. Each array is the pure signature of the six unmixing classes, obtained by the band pairing with aerial endmembers

OUTPUTS

- PRISMA tree's mask: satellite binary mask of tree's crowns (1 for tree's pixels, and 0 for non-trees)

3.4. Vegetation Indexes Extraction

The index extraction phase, is the main step of the workflow chain, as vegetation indexes are calculated in the zones with trees presence, to infer their health status. The main pipeline is summarized in Figure 3.14

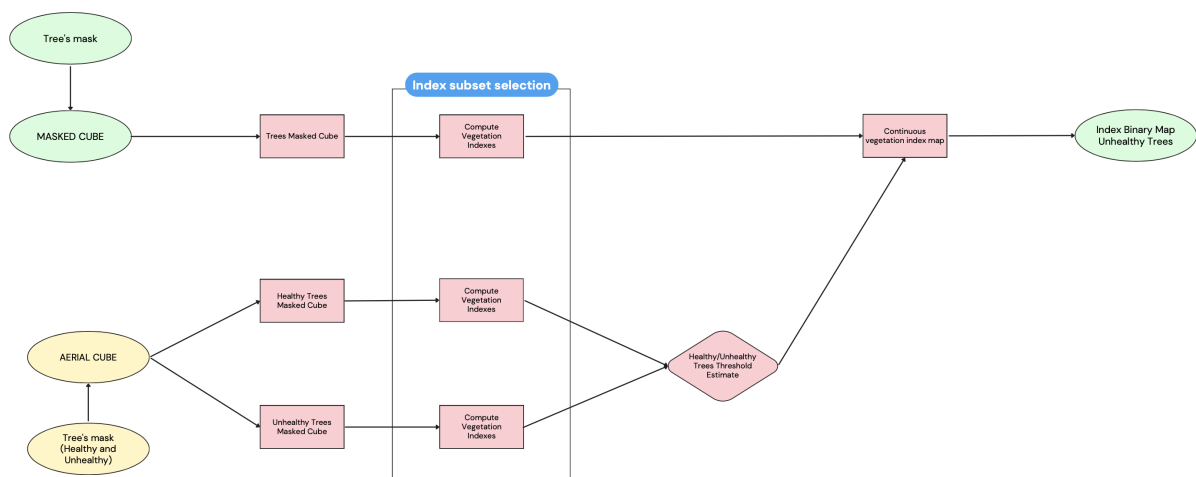


Figure 3.14: Vegetation Index Extraction workflow schema

3.4.1. Threshold extraction on asiaFENIX data

Since area 5 of the aerial data set is used as training input for the analysis, the starting point of this step is masking the aerial reflectance cube (of area 5), with the healthy and unhealthy trees' mask obtained from the unmixing procedure (chapter 3.3). Once done, the result will be a set of two reflectance datacubes, one with only reflectance value belonging to healthy trees and the other with just unhealthy ones.

After that, datacubes are ready to be processed in order to obtain vegetation indexes. To select the best suitable indexes to assess a possible bark beetle attack, a subset of the most influential indexes have been extracted from the collection of the ones present in the State of the Art of this study (chapter 2). The selection has been carried out accordingly to the result of [7], in which a Feature selection over several indexes was realized using the sequential floating forward selection (SFFS) method as the search strategy and a separability measure for the accuracy of the wSVM classifier after cross-validation on the training set. Conforming to [7], the feature selection algorithm selected eight indexes for the classification: CLRE, GNDVI, NBRI, NDREI, NDVI, NRVI, REIP and SLAVI.

The only index that didn't produce meaningful results for the study is REIP. As a matter of fact, the value distributions of healthy and unhealthy vegetation didn't show a clear separation, which resulted in the impossibility to set a proper threshold for this index (as will be explained later in this Chapter). Each of these seven indexes (neglecting REIP), has been computed by implementing a Python function on both reflectance cubes (healthy and unhealthy datacube).

This separated approach allowed to perform independent statistics over the healthy and unhealthy data sets, giving more insight into the values assumed by the two different categories. As a matter of fact, a random sample of pixels has been extracted from both healthy and unhealthy index maps for each index in the subset, and a histogram of the corresponding values has been produced.

The size of the random sample has been selected accordingly to Cochran's equation for large populations, selecting a proper precision level and confidence (formula 3.3).

$$n_0 = \frac{Z^2 pq}{e^2} \quad (3.3)$$

Where:

- e : is the desired level of precision (i.e. the margin of error)
- p : is the (estimated) proportion of the population which has the attribute in question,

- q : is $1 - p$.

As the final objective of index extraction is to create a binary map for unhealthy (or dead) trees for each of the seven indexes computed from the satellite data, the last step in the asiaFENIX chain is to find a suitable threshold to binarize satellite index maps, starting from some tuning based on the aerial area 5.

Each threshold is computed by calculating the intersection between the distribution of samples from healthy and unhealthy trees, for each one of the seven aerial index maps (Results of the procedure are reported in Section 4.3).

INPUTS

- Aerial reflectance cube: output of the previous pre-processing step
- asiaFENIX trees' masks (one for healthy and one for unhealthy trees): output of the previous unmixing step

OUTPUTS

- Vegetation map threshold: seven thresholds (one for each index of the subset selection), used to binarize satellite index maps

3.4.2. Index binary map production from PRISMA data

For PRISMA the index extraction pipeline is the same as the aerial one up to the index computation. Therefore, the 30kmx30km reflectance tile is masked through the binary trees' mask (which in this case it is just a single mask, summing up healthy and unhealthy trees). The seven indexes from the index selection are then computed on the aforementioned reflectance cube, producing seven index maps. As anticipated in Section 3.4.1, each index map is then binarized through a threshold computed from a statistical analysis of aerial data (area 5). Being these indexes a measure of the vegetation health, each pixel lower than the threshold will be assigned a value of 1, which stands for unhealthy trees, while all the others will be given a value of 0, which represents a healthy tree. The only exception is made for the CLRE (Chlorophyll Red Edge Index) which differently from all the other seven indexes decreases with the health state of the tree since it is sensible to the red edge band, which is an indicator of plant stress. For this particular case only, the value of 1 (unhealthy) will be assigned to pixels exceeding the threshold.

INPUTS

- PRISMA reflectance cube: output of the previous pre-processing step
- PRISMA trees' mask: output of the previous unmixing step

OUTPUTS

- Vegetation index binary maps for unhealthy trees: 7 binary maps (one for each index in the subset), underling the presence of unhealthy trees

3.5. Frequency Analysis

The last step before data validation is the frequency analysis, where for each pixel it is computed the frequency with which the threshold is exceeded in the seven thresholded index maps. More accurately, all the seven binary maps obtained from the previous Index Extraction step are summed together, so that the new map will assume values ranging from 0 (minimum frequency) to 7 (maximum frequency).

Since the resulting frequency map is composed of continuous integer values, it is crucial, in order to make results comparable with the aerial classification, to preserve the binary classification (0 for healthy and 1 for unhealthy). This last step is obtained (as can be appreciated from the schema in figure 3.15), by making use of a specific threshold. This threshold is selected with the same approach explained in section 3.9, which involves counting the percentage of unhealthy pixels in the validation classification map provided by the AVT AS company and replicating the same percentage of unhealthy pixels in the binary frequency map.

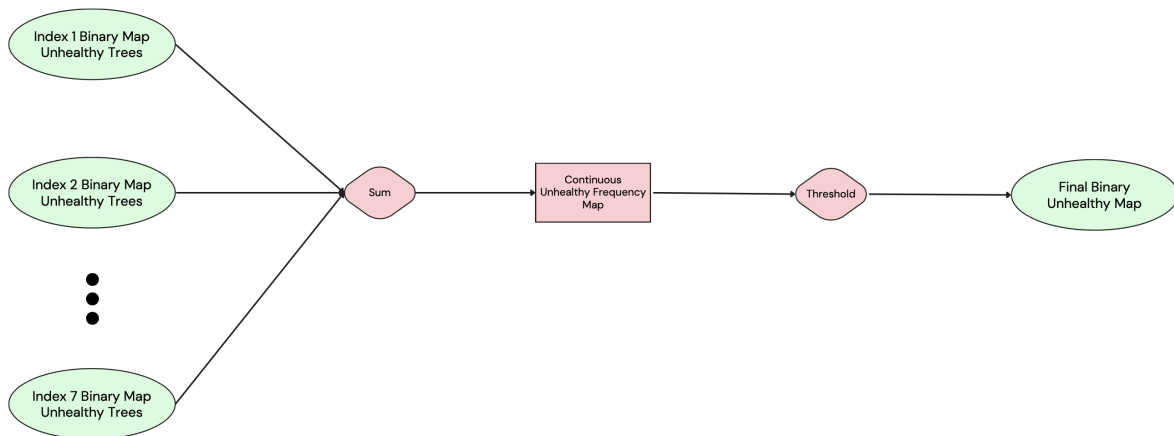


Figure 3.15: Frequency analysis workflow schema

INPUTS

- PRISMA index binary map: seven binary maps of unhealthy trees, outputs of the previous Vegetation Index Extraction step

OUTPUTS

- PRISMA final binary map: a single binary map that classifies unhealthy and healthy trees (with respectively 1 and 0)

3.6. Validation

The last step in the workflow pipeline is the validation of the results obtained from the satellite PRISMA data using as a reference the output of the AVT AS company aerial survey. Since area 5 (Figure 3.5) was used for training purposes, area 3 was devoted to validation (Figure 3.6).

The entire procedure involves mainly the processing of PRISMA images and it is resumed in Figure 3.16.

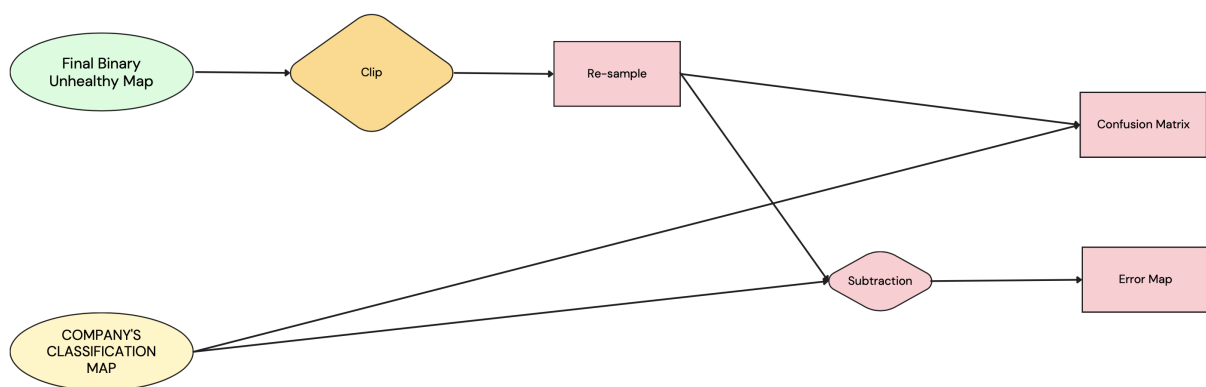


Figure 3.16: Frequency analysis workflow schema

Starting from the PRISMA output of the previous workflow step of Frequency Analysis (final binary mask of unhealthy trees), the map has been clipped in order to frame the same land portion of the aerial area 3. It is important to underline that this final binary map has been obtained, after the whole workflow procedure explained in the previous chapters, starting from data already coregistered with area 3, in the first step of preprocessing (explained in section 3.2.1). Because of that, the map is perfectly aligned with the aerial data after clipping.

Given the higher spatial resolution of aerial data, it is crucial to resample the satellite image to match the aerial resolution (from (20, 26) to (276, 360) pixel size).

Finally, the binary maps resulted from this study (obtained from PRISMA) were compared with the unhealthy binary maps extracted from the aerial survey classification map in two different ways:

- Creating a confusion matrix: to create a confusion matrix, satellite data is assigned to the predicted dataset, while aerial data is assigned to the actual one. Finally, the matrix counts the number of pixels corresponding to TP (True Positive), TN (True Negative), FP (False Positive) and FN (False Negatives), allowing to compute the accuracy and precision parameters, including the overall accuracy.
- Creating an error map: the error map is a spatial representation of TP, TN and misclassified pixels. It is obtained by a simple sum of the two actual and predicted binary maps, where values range between 0 and 2. The value of 0 corresponds to True Negative pixels, the value of 1 corresponds to misclassified pixels and 2 for True Positives.

INPUTS

- PRISMA final binary map: output of the previous frequency analysis step
- Aerial classification map: raster file that classifies area 3 of the survey accomplished by AVT AS company (as described in Chapter 3.1)

OUTPUTS

- Confusion matrix: confusion matrix of predicted values in the final satellite binary map
- error map: spatial distribution of TP, TN and misclassified pixel

4 | Results and comments

In the following section, the results of the different workflow steps will be presented separately. No distinction was made on the type of sensor since most of the results produced involve the combined analysis of data coming from both PRISMA and asiaFENIX.

4.1. Pre-Processing results

As anticipated in section 3.2.1, satellite data has been re-georeferenced (or coregistered), using aerial data of area 3 as reference. As already stated, the coregistration has been performed only with area 3, since only in the validation process binary maps will be superimposed to obtain the error maps. If double points were collected also from area 5, the coregistration would have taken into account double points' displacements from both areas, performing an averaged transformation, which would have been a more robust transformation against outliers, but producing a locally misaligned image with respect to area 3. The choice of co-registering with area 3 only was made since the purpose of the coregistration step is not to improve PRISMA's overall georeferentiation but to locally align the image with validation data in order to reduce the number of false positives and negatives.

Five different transformations have been explored following a k-fold cross-validation procedure, as already anticipated in Chapter 3.2.1.

This cross-validation procedure is very useful since it allows residuals to be affected by only one displacement. By averaging the results for k possible configurations, it is possible to take into account displacements in different portions of the image.

As a result, a total of seven tie points have been collected, where five of them have been kept for warping (fixed points) and the remaining two for the "leave one out" procedure. The spatial location of the seven tie points is represented in Figure 4.1 and 4.2, where respectively the first show those points in the PRISMA cube, while the second in the asiaFENIX one.



Figure 4.1: The set of 7 tie points selected for image coregistration on PRISMA image



Figure 4.2: The set of 7 double points selected for image coregistration on asiaFENIX image

As can be observed from Figure 4.2, points are mainly distributed on the borders of the aerial image. Moreover, from image 4.1 it is clear how the low resolution of PRISMA, makes features almost unrecognizable, therefore it has been possible to associate tie points, just by using the shape of the edges of the forest as reference points, which are mainly

located at the borders of the aerial acquisition. This limitation is also the reason why it was not possible to collect a higher number of tie points. In Table 4.1, the list of mean residuals for each transformation type is shown. Results have been averaged considering all the leave-one-out configurations. Units are reported in pixels and the criteria to choose the best transformation type is simply the selection of the method with the smallest mean residual. As a result, the Helmert method has been selected as the transformation type.

Mean error for each coregistration algorithm

	Mean residual
Linear transformation	1.04
Helmert	0.85
Polynomial of degree 1	0.92
Polynomial of degree 2	0.99
Projective transformation	0.92

Table 4.1: Pixel mean error for each transformation type (pixel units)

Finally, the effects of the coregistration procedure with the Helmert transformation can be appreciated from the before and after representation in Figure 4.3

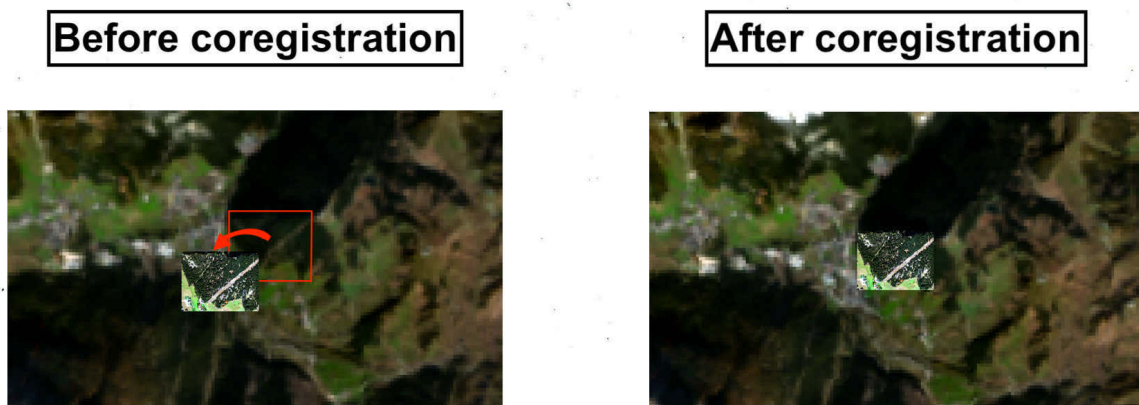


Figure 4.3: Before and after representation of the satellite image coregistration

Before coregistration, the two images are clearly misaligned, as can be evicted from the main features of the area: the forest and the unvegetated path crossing in the middle.

The co-registration is fundamental, since considering the significant error between the two acquisitions, a validation procedure wouldn't be possible without aligning the two images. The results show how after the coregistration procedure, the situation is visibly improved. Needless to say, the results are not perfect, as the coregistration procedure is performed with a low amount of double points, not evenly distributed in the image space. Although this may not result extremely accurate for other types of analysis (e.g. change detection), the solution is expected to provide sufficiently precise outcomes for a simple validation procedure considered in this work.

4.2. Unmixing results

The first results of the unmixing procedure are the asiaFENIX spectral signatures extracted from the ROIs of area 5 presented in Chapter 3.3.1 (Figure 3.10). The PRISMA satellite signatures are then obtained from a "band pairing" procedure, deeply explained in Section 3.3.2, which allows to average the reflectance between the aerial bands.

Trees signatures in Figure 4.4 are extremely coherent with the classical signatures of healthy vegetation. The reflectance, as can be observed from the graph, is generally absorbed in the visible range by healthy leaves, and reflected in the higher portion of the visible spectra, around the green and blue band [17]. The healthy vegetation usually experiences a strong response between the green and Near Infrared range, as confirmed in Figure 4.4.

As expected, the curve is almost flat to 0 in the SWIR region, as higher values in this portion are usually associated with low water content. Water, in fact, tends to absorb light in this region and if the vegetation is healthy, water content is usually higher [2].

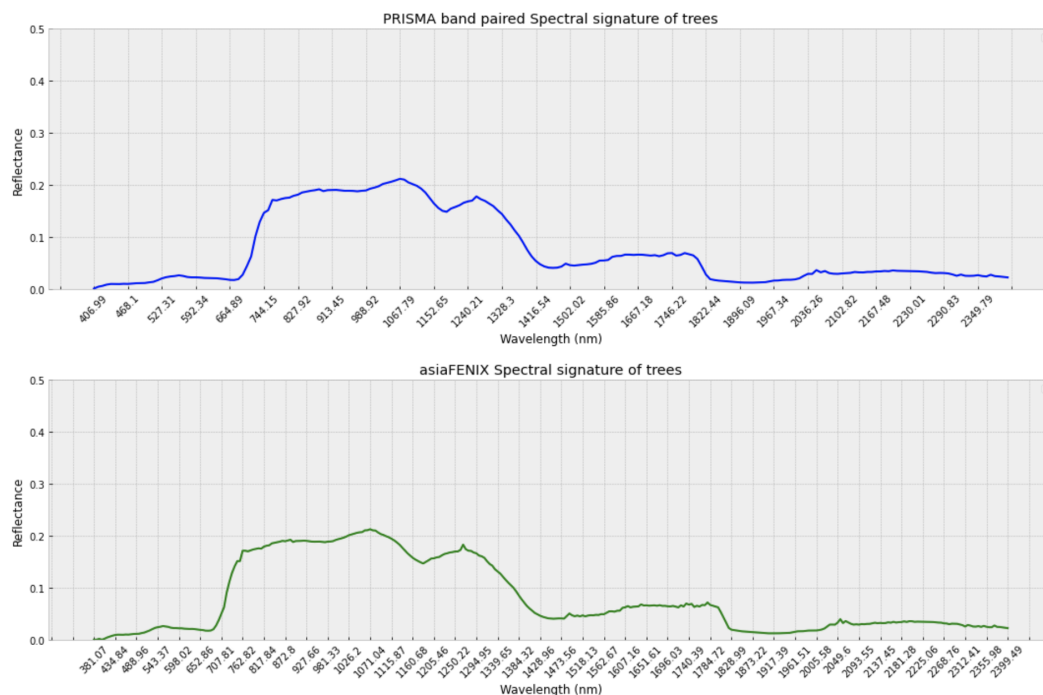


Figure 4.4: Healthy tree spectral signature of aerial sensor and PRISMA band paired version. The blue curve is used to represent the satellite signature, while green is used for the aerial one

By comparing the spectral signature of unhealthy trees with the healthy ones, it can be immediately noticed how the visible and NIR spectra trend is clearly flattened. While healthier trees (as well as grassland) see their reflectance increase around the green band (with a clear first increasing trend at 550-600nm, which becomes stable at a reflectance value of 0.2), unhealthy ones have a more constant trend in the visible and near-infrared. Despite this, the same peak observed in healthy trees can be appreciated at 1250nm. After this maximum, the curve is almost the same up to the middle of the SWIR spectra (1785nm), but after that unhealthy trees have a higher response up to 2500nm (with a reflectance constant value of 0.1), while the response of healthy trees is almost absent.

As known from the literature, vegetation health is characterized by a good response in the visible and NIR spectra, and this explains the flattening trend experience in this region by unhealthy trees. At the same time, as anticipated, both curves have a peak around 1250nm. This region, at the border of NIR and SWIR, is commonly used to assess the type of vegetation, which is totally coherent with the fact that independently from their health, both classes belong predominantly to the category of Spruce trees.

Moreover, the lower reflectance values in the SWIR region are consistent with the expectations since the absence of water in unhealthy vegetation allows for higher reflection (less

absorption) of light in this spectrum range.

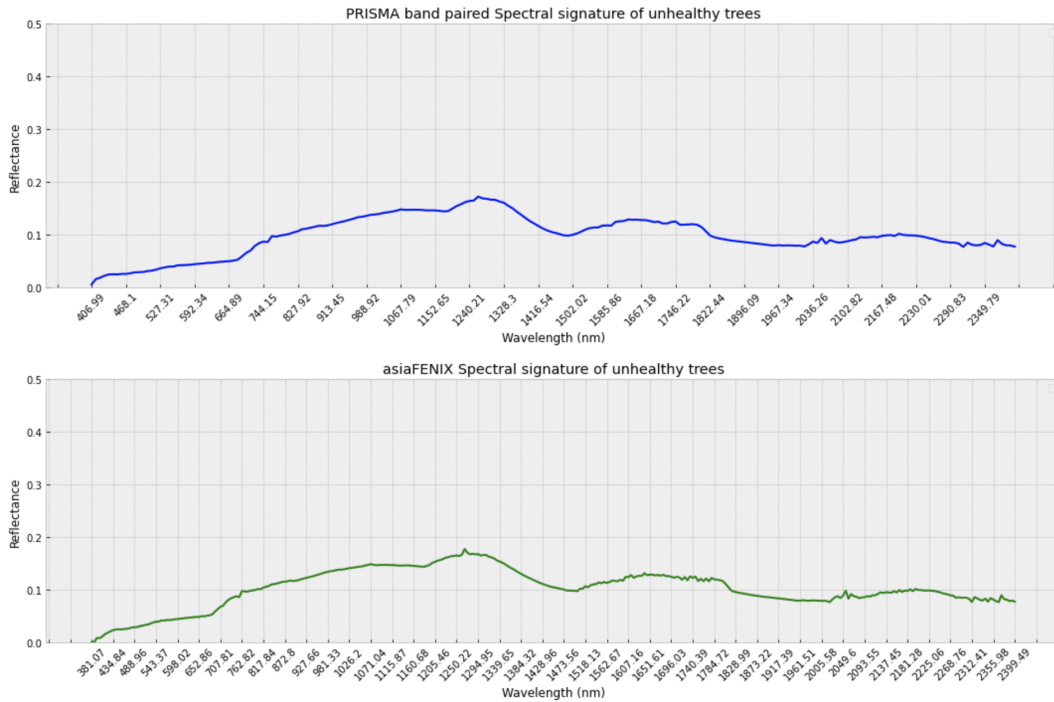


Figure 4.5: Unhealthy tree spectral signature of aerial sensor and PRISMA band paired version. The blue curve is used to represent the satellite signature, while green is used for the aerial one

Since the objective of unmixing is to depict tree canopy abundances per pixel, in order to extract binary trees' masks, it was chosen to select a restricted amount of classes. This choice is justified by the fact that to properly define the boundaries of trees' zones, it is important to have a small amount of well-distinct classes. For this reason, some of these next signatures may contain more than one category of land under the same class.

With the term "unvegetated area", it has been decided to encompass all those categories which do not belong to vegetation: river bed, bare soil, rocks, and artificial surfaces (buildings and roads). The curve in Figure 4.6 reflects the usual trend of soil [14] in the first part of the visible and NIR portion, while it shows signs of a faint reflectance decline in the SWIR spectra, more common of artificial surface signatures [33].

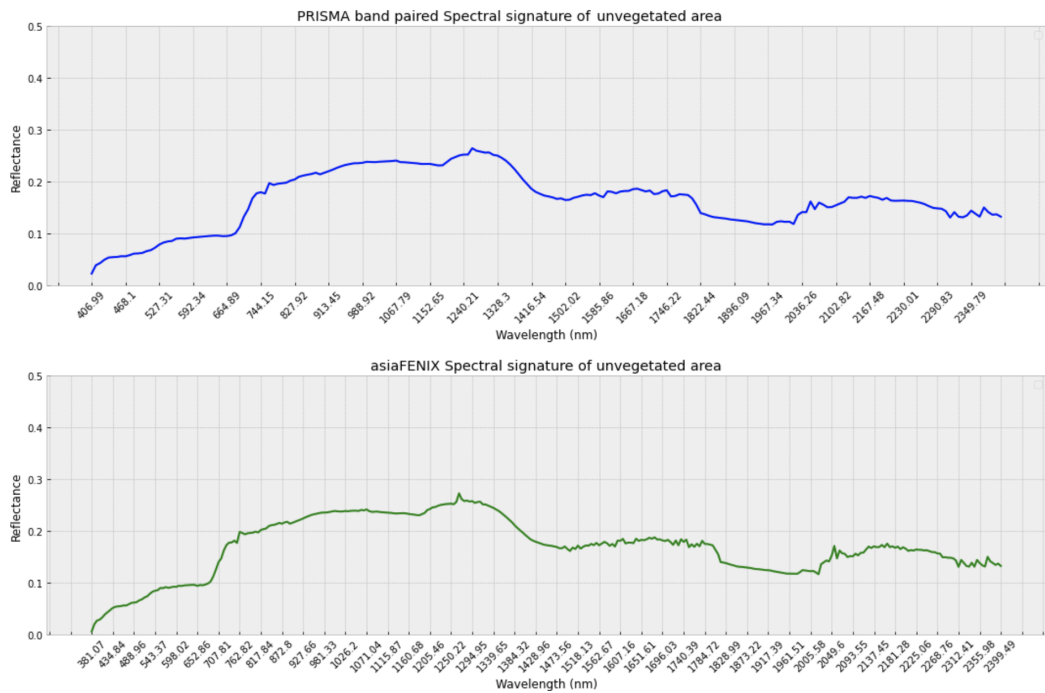


Figure 4.6: Unvegetated area spectral signature of aerial sensor and PRISMA band paired version. The blue curve is used to represent the satellite signature, while green is used for the aerial one

Grassland class falls into that category of green vegetation, which not includes trees (e.g. grass or small green plants). Figure 4.7 shows even greater similarity to the healthy vegetation signatures trend, with respect to the trees' signature seen in the previous lines. This is something that can be expected, as trees may contain mixed pixels composed of wood or shadow (in addition to canopy), which can affect the pure signature distribution over the spectra.

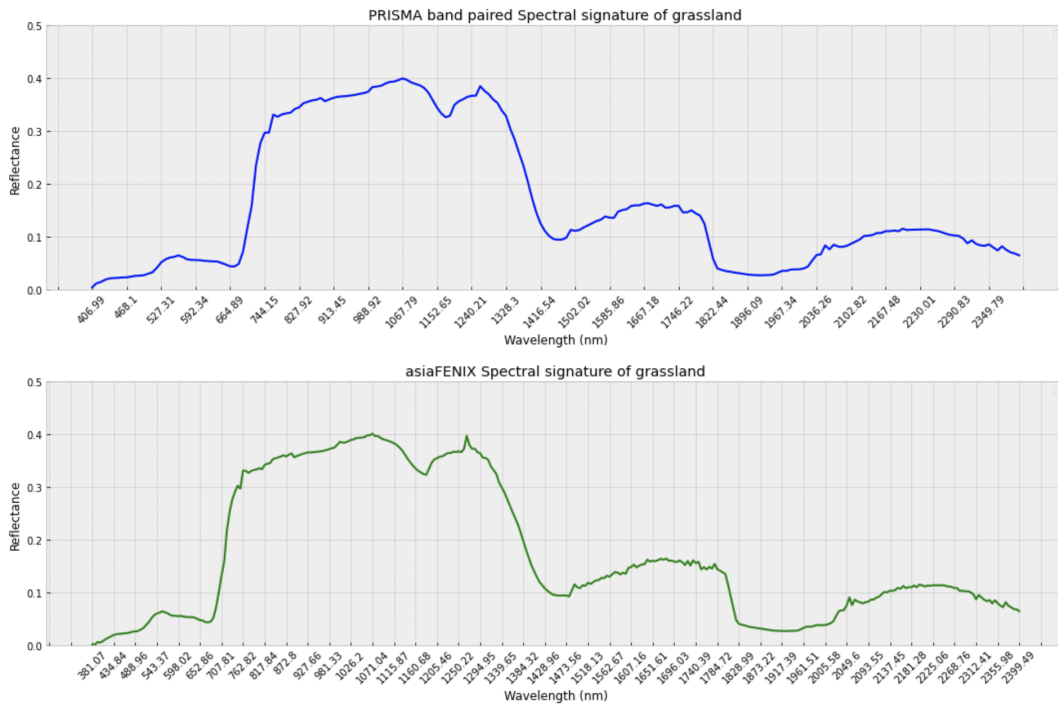


Figure 4.7: Grassland spectral signature of aerial sensor and PRISMA band paired version. The blue curve is used to represent the satellite signature, while green is used for the aerial one

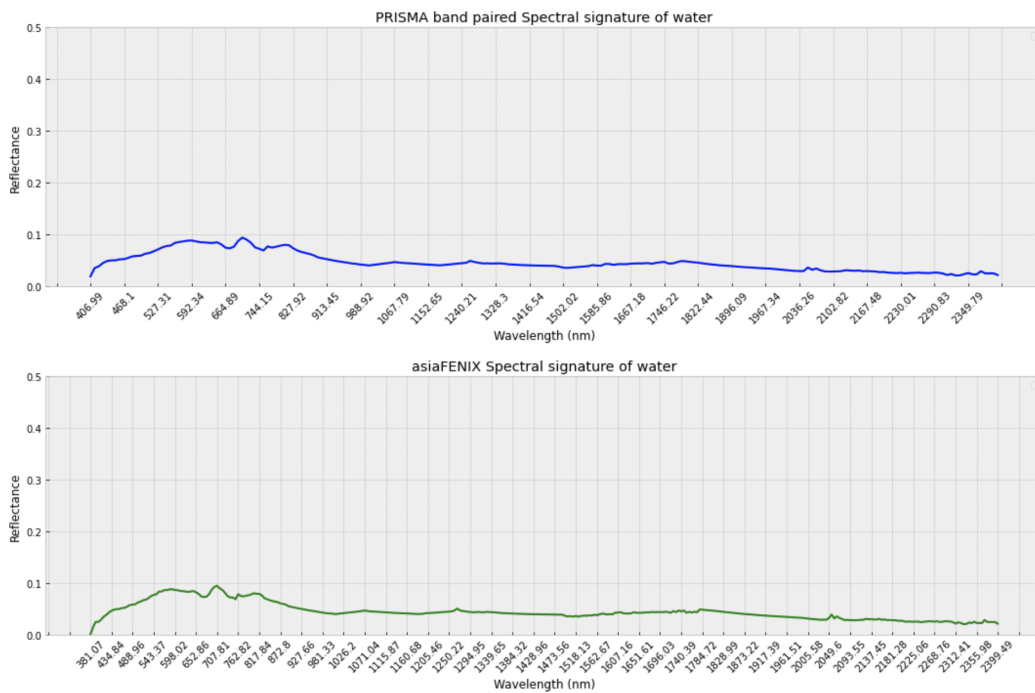


Figure 4.8: Water spectral signature of aerial sensor and PRISMA band paired version

Regarding water and shadow in Figure 4.8 and 4.9, it is possible to appreciate a very similar curve, with values always almost close to zero, because of the absence of light scattering.

The only difference is a weak response in the low portion of the visible spectra of water, which matches with literature results [25].

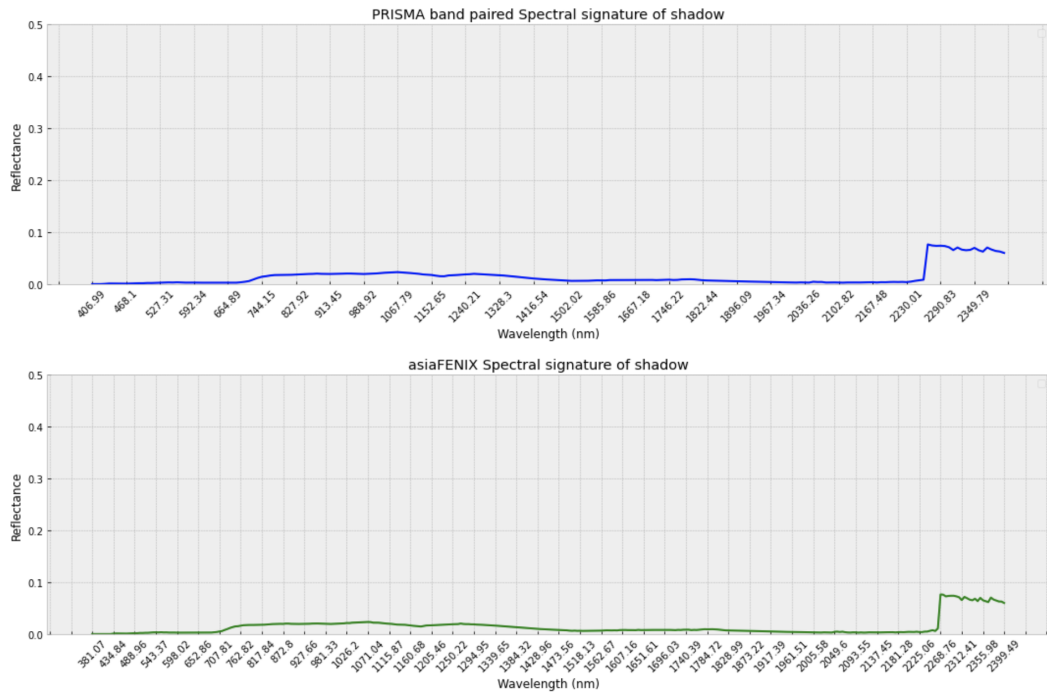


Figure 4.9: Shadow spectral signature of aerial sensor and PRISMA band paired version. The blue curve is used to represent the satellite signature, while green is used for the aerial one

Finally, it can be noticed for all spectral classes, that the PRISMA band paired signatures follow the same pattern as the aerial ones, proving the right operating principle of the "band pairing procedure".

Once satellite band-paired spectral signatures have been produced, they are used as input for the Unmixing procedure to produce abundance maps. The complete results for the entire 30km x 30km tile are reported in Figure 4.10. Without a closer look at the single study areas, it is quite hard to understand the effectiveness of those maps, due to the large coverage of the sensor (images frame a big portion of land). Despite this, by a quick comparison with the RGB representation in Figure 3.4, it is possible to infer that the algorithm is correctly identifying the shadows, which appear as black areas in the RGB. Concerning the unvegetated area, a village at the top left of the acquisition is correctly detected from the maps, as well as snow which is correctly identified as a non-vegetated

area. On the other side, the remaining classes need to be further inspected from a closer look at the training and validation area.

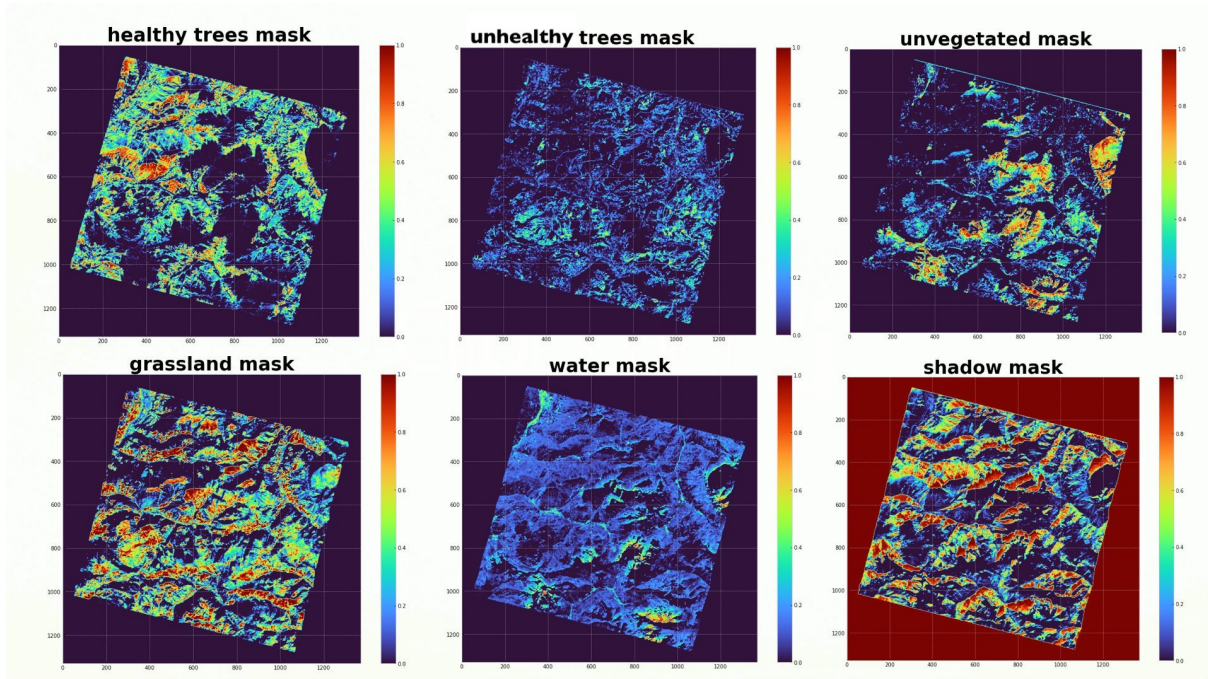


Figure 4.10: PRISMA abundance maps of the entire 30km² acquisition tile

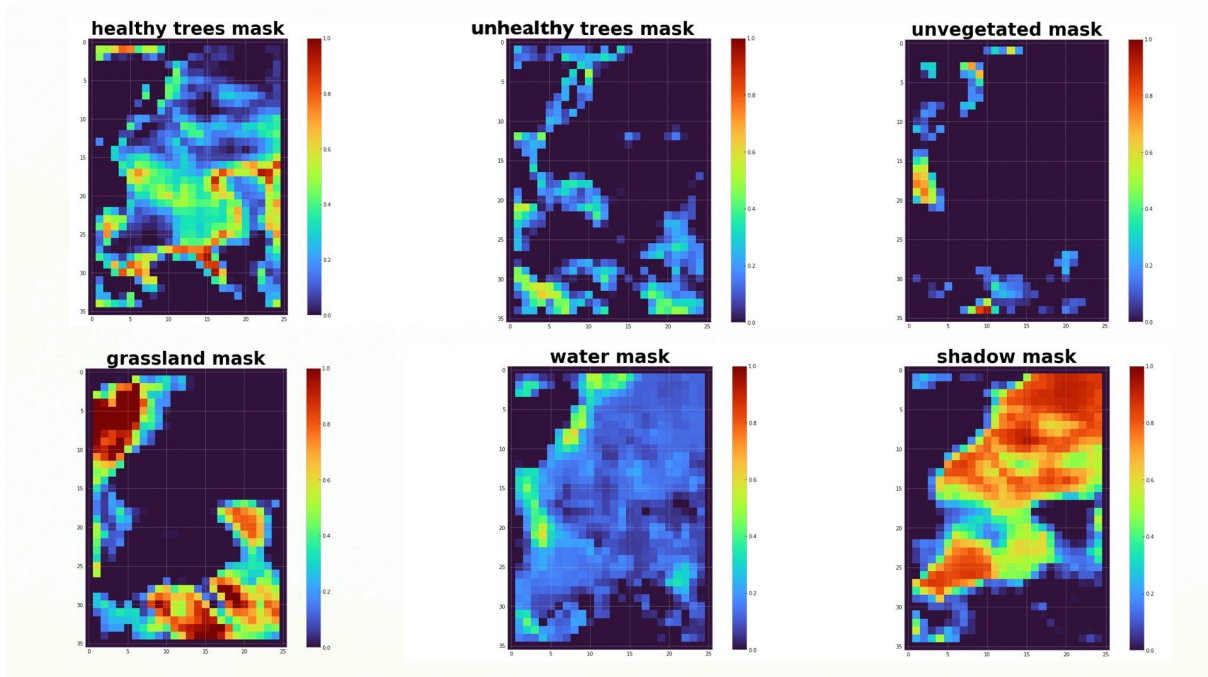


Figure 4.11: PRISMA abundance maps of area 5

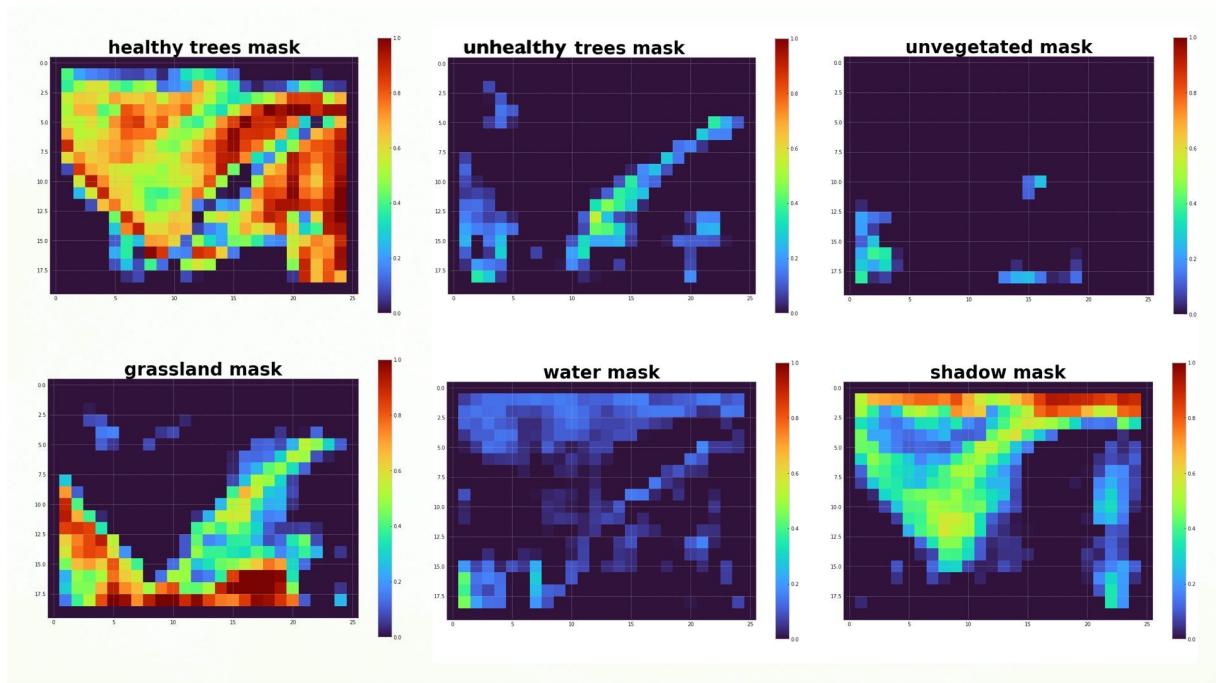


Figure 4.12: PRISMA abundance of area 3

In both cases (areas 3 and 5), a significant amount of healthy trees' crowns seem to be properly detected by a high tree abundance, depicting an accurate boundary with grassland, which is also precisely identified by the algorithm. However, due to the coarse spatial resolution of the PRISMA image, it is visibly hard for the algorithm to outline the small shadow areas that are included inside the forest. As a matter of fact, by a close look at both areas 5 and 3, it can be evicted how the shadow abundances are not properly isolated, but on the contrary, they are quite spread in the trees' crown area. This situation is quite comprehensible, considering that the spatial resolution of the satellite is 30m, while the size of the smallest shadow holes in the aerial acquisition doesn't exceed the meter level (as can be observed from the unclassified and shadow areas in the aerial classification map in Figure 3.2 and 3.1).

After producing the abundance maps, the algorithm automatically extracts, from a quick analysis of the classification map of the training area (area 5), the exact number of pixels and produces the percentage of unhealthy pixels to use as a threshold for the abundance map binarization: 39%. The results of the entire PRISMA acquisition are collected in Figure 4.13.

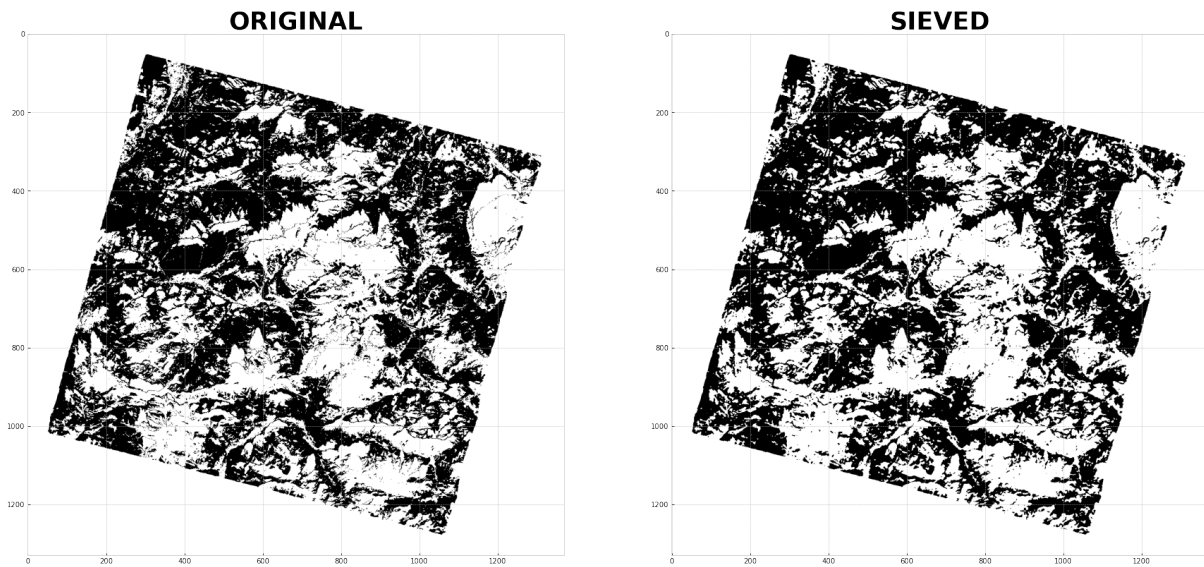


Figure 4.13: PRISMA binary maps of trees (healthy and unhealthy together) before and after sieving

The last step is the sieving of the mask, to remove possible salt and pepper effects. For this study, it has chosen to apply a median blur filter with a kernel size of 3. On the right side of Figure 4.13, the effects of sieving are voluntarily slightly noticeable, since with such a small kernel size, it will be possible to filter out just the finest imperfections at the pixel level (which may be generated by outliers).

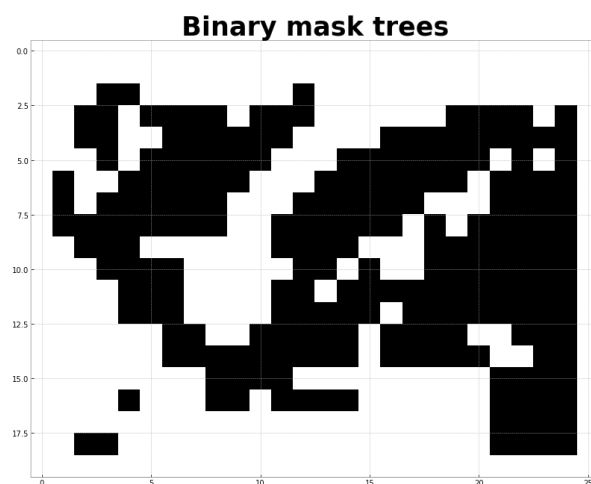


Figure 4.14: PRISMA binary maps of trees (healthy and unhealthy together) of area 3

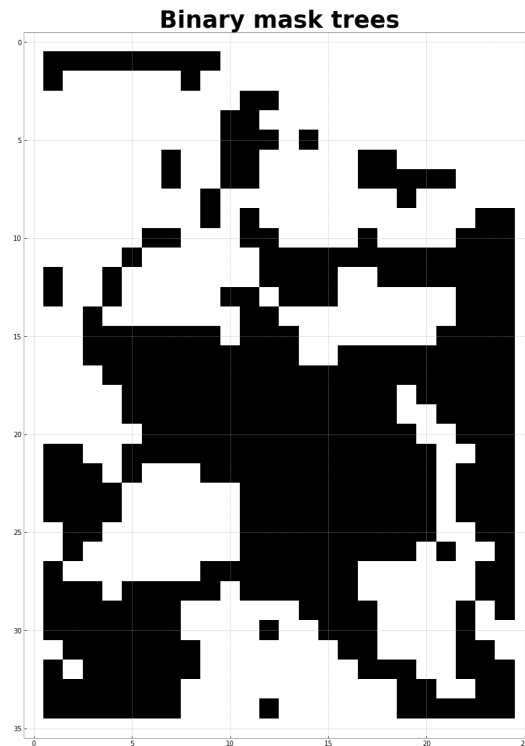


Figure 4.15: PRISMA binary maps of trees (healthy and unhealthy together) of area 5

After observing the zoom on the binary map produced on the validation and training area, it is possible to appreciate how the aforementioned phenomenon of shadow overestimation in the abundance maps is propagated to the binary results. Despite this, the majority of the trees' crowns are still identified by the algorithm.

Finally, to produce the training input for the spectral index extraction step, the same process is replicated for aerial images of area 5, but in this case, two different binary maps will be produced instead of one. The first map is a mask for healthy trees, while the second corresponds to unhealthy ones. The results are reported in the following figures (figure 4.17 and 4.16), and they are proving the higher effectiveness of this algorithm with higher spatial resolution data.

From a quick inspection of the areas detected by the binary mask in Figure 4.17, it can be discovered a close similarity to the stressed areas detected by the survey of the "AVT AS" company in Figure 3.1

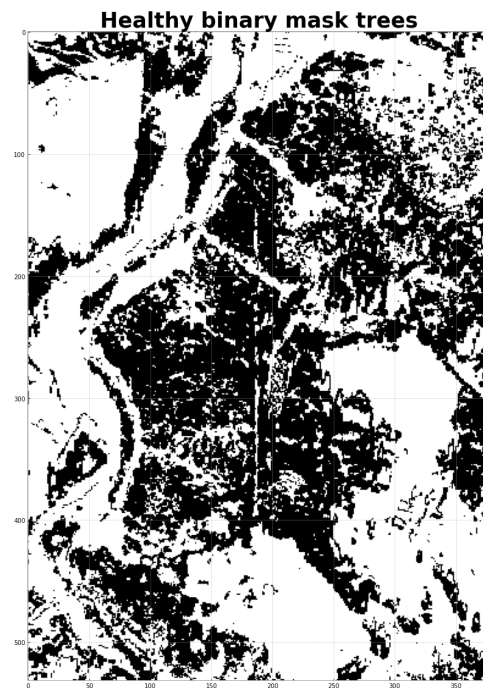


Figure 4.16: Binary mask of healthy trees of area5, extracted from aerial data for training purposes

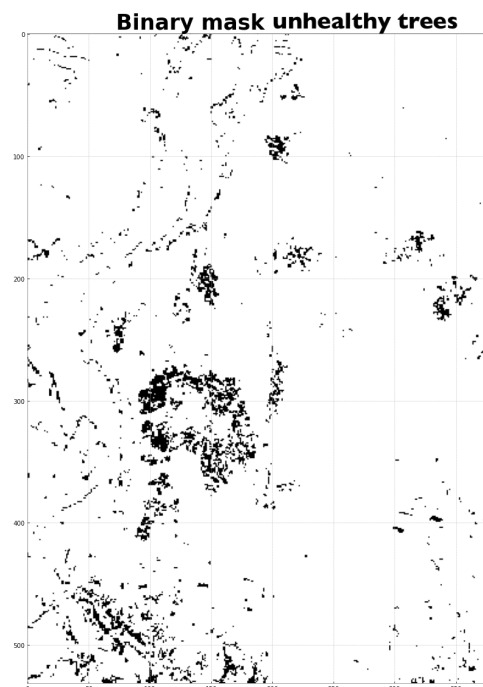


Figure 4.17: binary mask of unhealthy trees of area 5, extracted from aerial data for training purposes

4.3. Spectral Indexes Extraction results

Before inspecting each PRISMA spectral vegetation index and analysing its spatial distribution in a map, it is important to work on aerial data to produce training inputs. In the first place, the binary maps obtained from the previous Unmixing step (Figure 4.17 and 4.16) are used to separately compute the vegetation indexes on aerial data for healthy and unhealthy trees. In the two maps in Figure 4.18, it can be appreciated one example of vegetation index (in particular NDVI). This example, clearly explains how the two tree classes exhibit different clusters of NDVI values, which are closer to 1 in healthier vegetation and to 0 in unhealthier trees.

Since the aim of this chapter is to obtain results from the satellite data, the same vegetation map is reproduced with the PRISMA acquisitions, for each of the seven indexes.

The next step in the chain is the binarization of each satellite vegetation map. To this aim, a proper threshold needs to be selected. First of all, the aerial vegetation index value distribution of area 5, split by unhealthy and healthy class, are plotted into the same graph, as shown in Figures 4.19, 4.20, 4.21 and 4.22. Those values are extracted from a random sample of pixels from the healthy and unhealthy class, by following Cochran's formula, explained in section 3.4.1. Therefore, considering a total population of 201628 (total number of pixels in area 5 aerial acquisition), a confidence level of 95% and a precision level of 3%, the optimal sample turned out to be 1068 pixels by class.

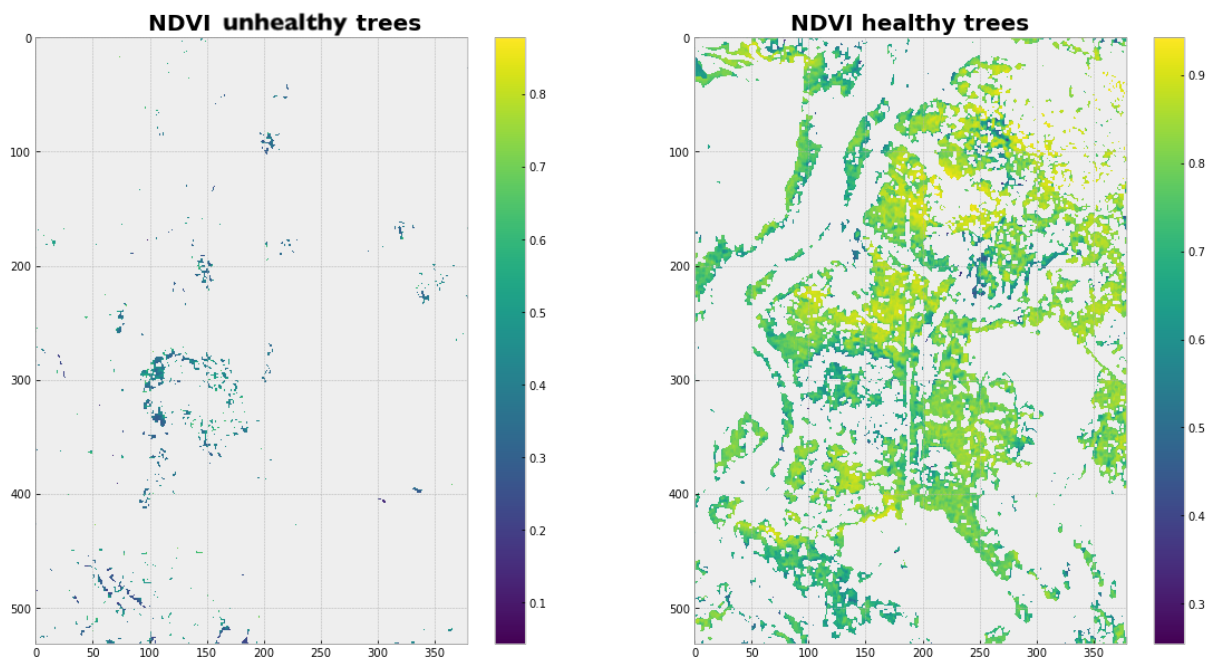


Figure 4.18: NDVI aerial vegetation maps example used for training

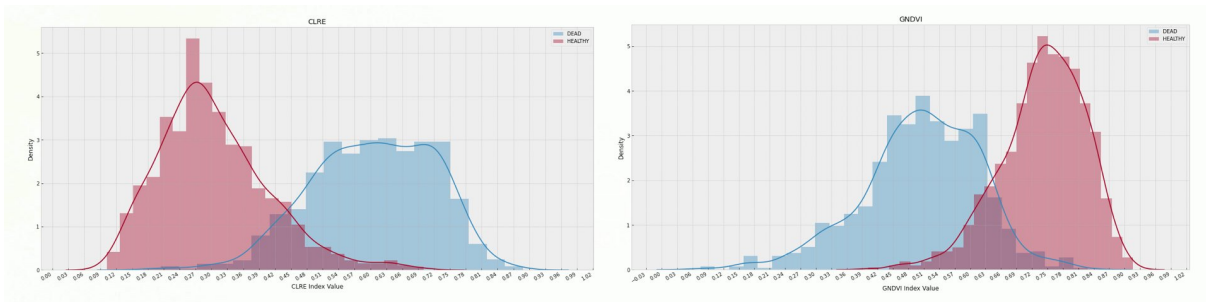


Figure 4.19: CLRE and GNDVI values distribution for healthy and unhealthy trees in random sample

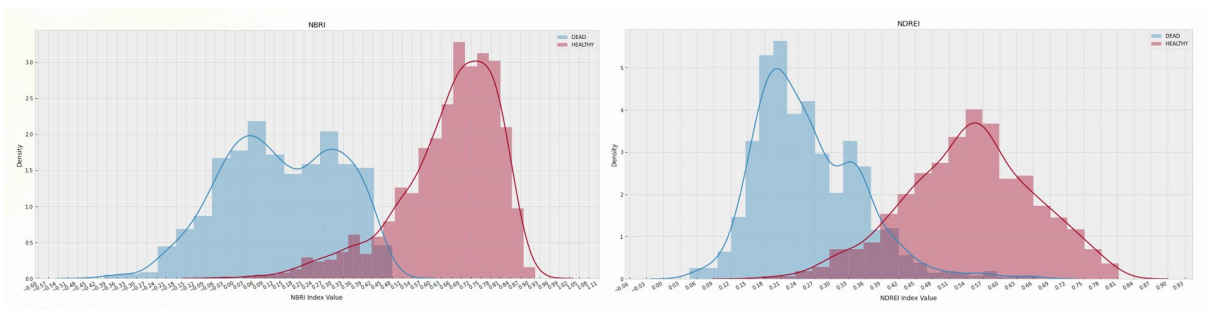


Figure 4.20: NBRI and NDREI values distribution for healthy and unhealthy trees in random sample

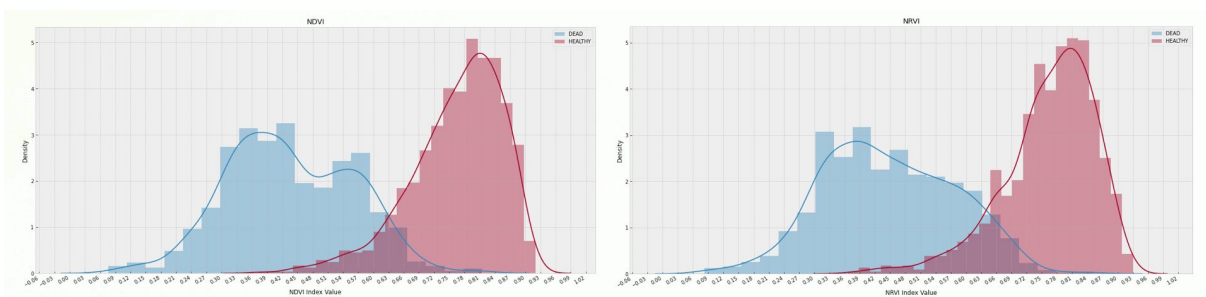


Figure 4.21: NDVI and NRVI values distribution for healthy and unhealthy trees in random sample

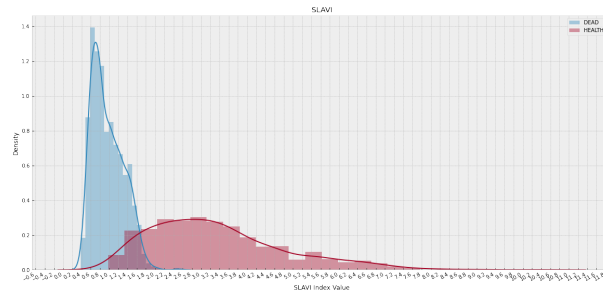


Figure 4.22: SLAVI values distribution for healthy and unhealthy trees in random sample

In each graph, it can be appreciated a sharp separation of the two distributions, which bodes well for the threshold extraction. As a matter of fact, the binarization threshold is inferred from aerial data by looking at the intersection of the two distributions and extracting the index value corresponding to this junction point.

From a brief look at the distributions it stands out how, differently from all the other six indexes, CLRE is the only index where the healthy distribution precedes the unhealthy one in the graph. As anticipated in Chapter 3.4.2, this phenomenon finds confirmation in literature, being CLRE directly proportional to the stress of the vegetation (instead of the health, like all the other six indexes). The thresholds gathered from each index vegetation map are reported in Table 4.2.

Mean error for each coregistration algorithm

	Threshold
CLRE	0.44
GNDVI	0.64
NBRI	0.44
NDREI	0.39
NDVI	0.63
NRVI	0.64
SLAVI	1.7

Table 4.2: Threshold selected for each index vegetation map binarization

Finally, each of these aerial thresholds is applied to its relative PRISMA satellite index vegetation map, obtaining the corresponding binary representation in Figure 4.23. The

entire set of index maps seems to provide various and useful insights to the analysis, with the only exception of the NDREI index, since its patterns appear really similar to the general binary tree map in Figure 4.13.

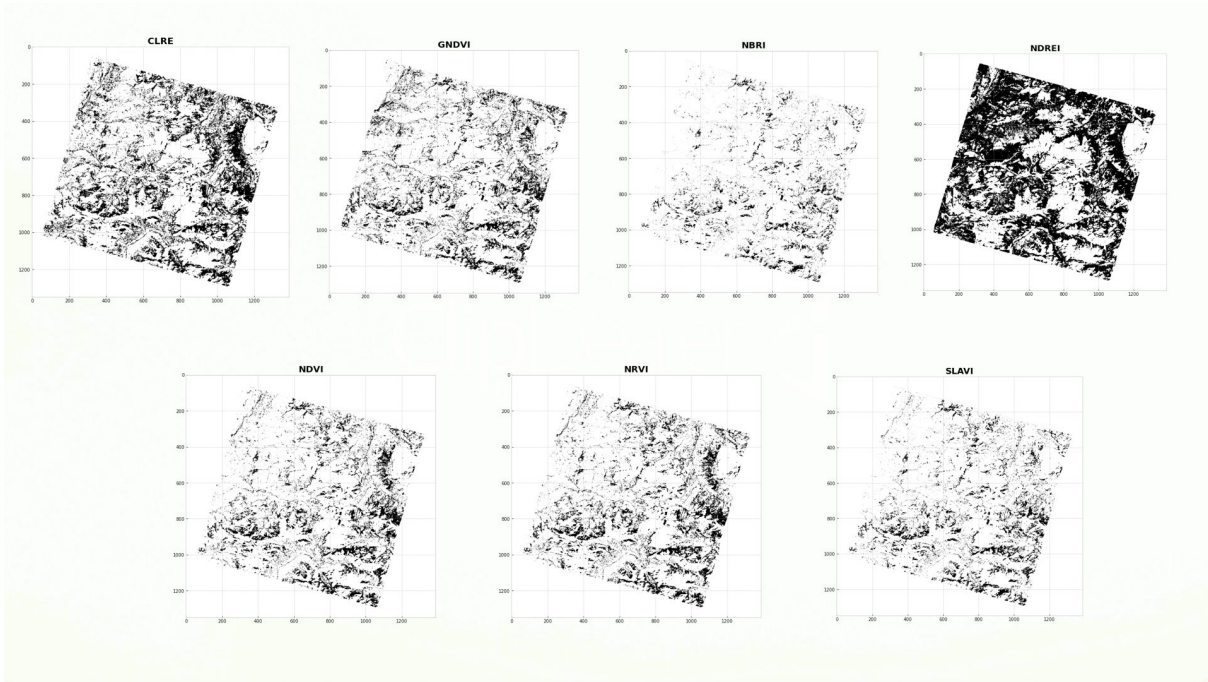


Figure 4.23: PRISMA vegetation index maps binarized with the threshold. In black are represented pixels exceeding the threshold (pixels with a higher risk of being unhealthy trees) and in white healthy trees or pixels masked out by the trees mask

4.4. Frequency Analysis results

By performing the addition of all the seven index binary maps, it is possible to evaluate the frequency of trees' exposure to possible stresses (e.g. Bark Beetle attack). On the left side of Figure 4.24 it is reported the index map computed on the entire PRISMA acquisition. On the right, instead, a binary map is extracted from the same frequency map, by selecting the 39% of the pixels with the highest frequency (to replicate the same percentage of unhealthy trees' pixels of the aerial classification map as explained in Section 3.3.1). Judging from this first result, it appears that the zones most subjected to Beetle's attacks are mostly located toward the east and south of the interested area. Nevertheless, it is important, in order to have a first proper visual feedback, to compare this data with existing classifications. As a matter of fact, a closer look at areas 5 and 3, can potentially help with a first high-level validation (Figure 4.25 and 4.25).

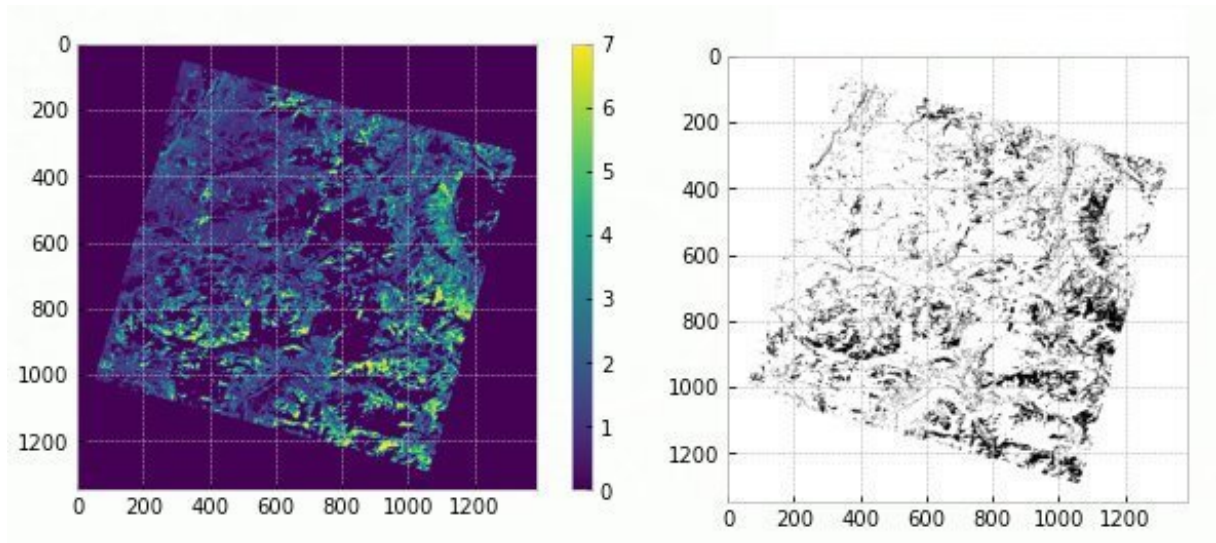


Figure 4.24: On the left side, the frequency map of unhealthy trees, where each pixel value corresponds to the number of indexes that exceeded the threshold in the spectral index analysis. On the right side, the binarized frequency map, where black pixels correspond to the 39% of the pixels with the highest frequency.

Comparing these results with the aerial classification data (Figure 3.1 and 3.2), it can be pointed out that the algorithm is more prone to detect larger unhealthy areas, if compared to the aerial classification. This behaviour is totally expected, considering the difference in scale between the two sensors' spatial resolutions (almost 1:15). In particular, the large spot detected by the algorithm located approximately at [10,20] (pixel coordinates) in Figure 4.25, finds confirmation in the AVT AS classification (in Figure 3.1). However, the satellite results are showing some erroneous detections over the river borders (northwest side of the acquisition at about [10,10]). This is imputable to the small size of the river cross-section with respect to the PRISMA spatial resolution, which caused the generation of a too much generous tree's mask contour in the unmixing phase.

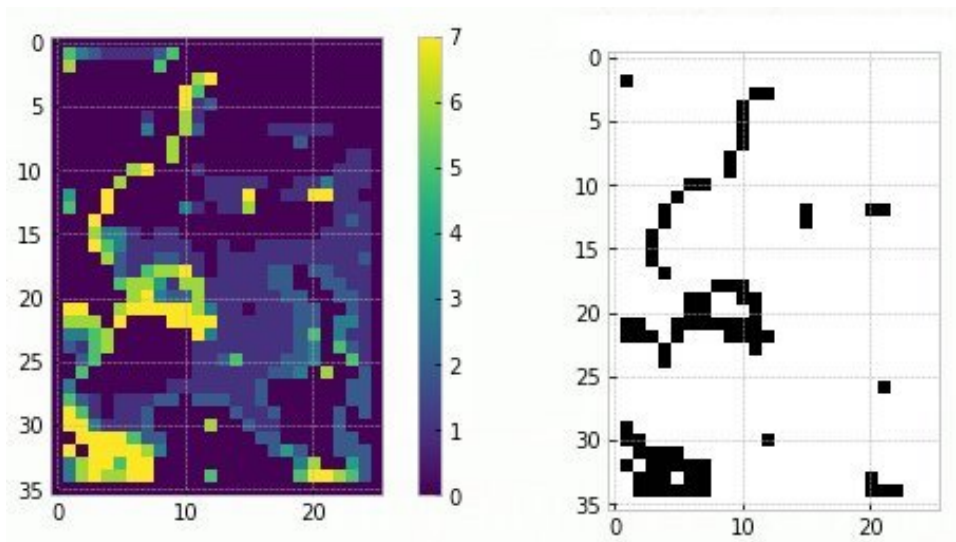


Figure 4.25: On the left side, frequency map of unhealthy trees in area 5, where each pixel value corresponds to the number of indexes that exceeded the threshold in the spectral index analysis. On the right side, the binarized frequency map, where black pixels correspond to the 39% of the pixels with the highest frequency.

Regarding area 3 the situation is totally different, as the unhealthy trees' spots in the aerial validation map (Figure 3.2) are far smaller than the actual satellite's GSD. For this reason, it is quite difficult to assess results from a qualitative comparison with the classification map, as the map is not able to replicate such a local effect on the vegetation.

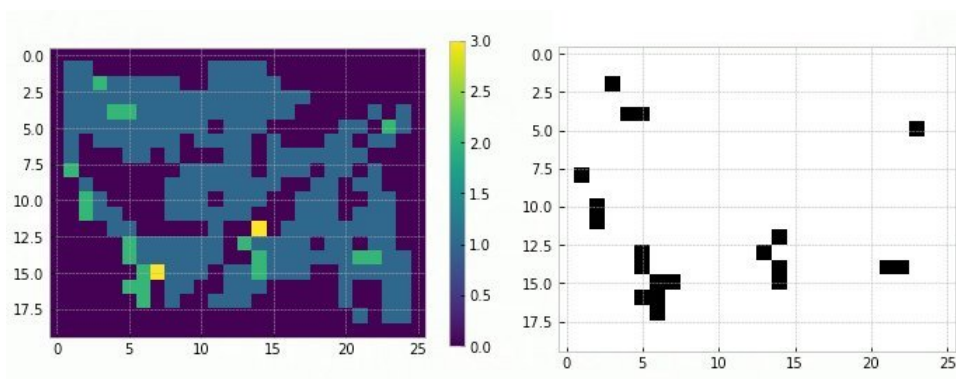


Figure 4.26: On the left side, frequency map of unhealthy trees in area 3, where each pixel value corresponds to the number of indexes that exceeded the threshold in the spectral index analysis. On the right side, the binarized frequency map, where black pixels correspond to the 39% of the pixels with the highest frequency.

4.5. Validation results

In this section, only the results of area 3 will be considered allowed for validation, since this is the only area that has not been used for model training. Results of area 5 are presented just for comparison and commenting purposes.

The validation binary map in figure 4.27, is extracted from the classification data provided by the AVT AS company (Figure 3.2).

The first step to perform a proper validation, is the resample of the PRISMA images, in order to match the aerial resolution. Images are upsampled from a size of (20, 26) to a size of (276, 360), with a Nearest Neighbor interpolation. The choice of upsampling lower-resolution images to higher-resolution ones (and not the way around) is made with the purpose of preserving the shape of the detected areas by PRISMA, by increasing only the number of pixels. By downscaling the aerial image, on the other side, the pixel content would have been averaged, hence altering the shape of the aerial acquisition.

The upscaled PRISMA image and the validation map (area 3) are shown in Figure 4.27

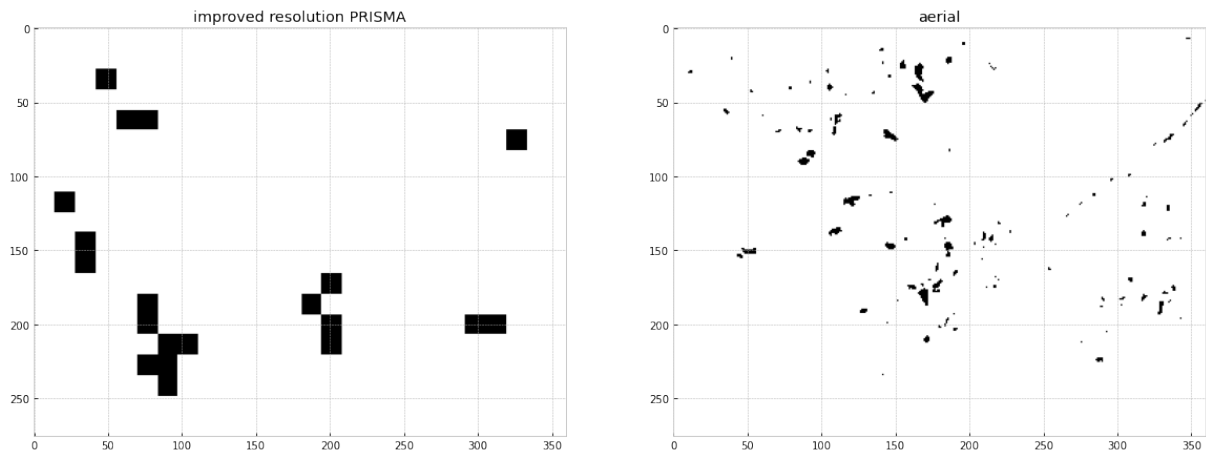


Figure 4.27: On the left, resampled PRISMA frequency binary map. On the right, aerial validation binary map (area 3)

The statistics of the prediction performed by the algorithm on satellite data are collected in a confusion matrix, obtained by superimposing the two images and comparing the predicted results (PRISMA) with the actual ones (asiaFENIX). Results are reported in Figure 4.28

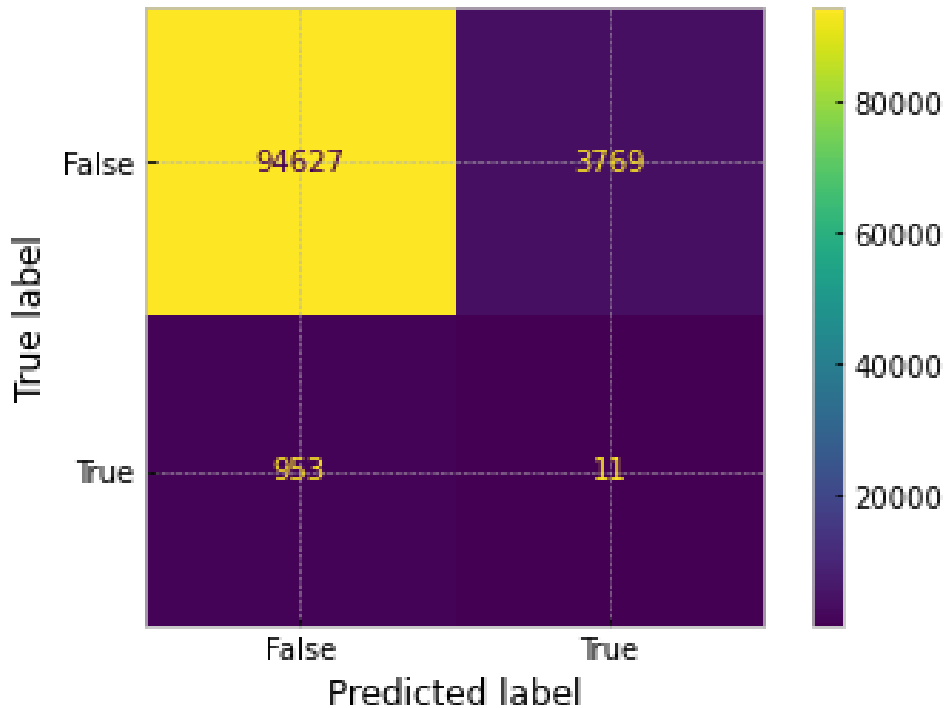


Figure 4.28: Confusion matrix of the satellite prediction over the validation area (area 3)

The model produced is performing with an accuracy of 95% and a precision of less than 1%. These results are not surprising, considering the nature of the validation data. As a matter of fact, the percentage of unhealthy trees in the validation area is highly smaller with respect to the training one. In area 3 only less than 1% of the pixels are unhealthy trees, which is even smaller than the 4% of area 5. Moreover, the accuracy level is able to reach such a high percentage, due to the high number of True Negatives (corresponding to healthy and non-tree zones) that are correctly detected by PRISMA. Since the amount of unhealthy trees is so scarce, the performance of the detection of healthy vegetation is necessarily boosted.

Moreover, in addition to the lack of unhealthy data, unhealthy pixels are also unevenly distributed over the map, which makes the detection for a 30m satellite impossible, as it would require making detections under the pixel level (as anticipated in the previous chapter). This causes a strong decline in the precision level.

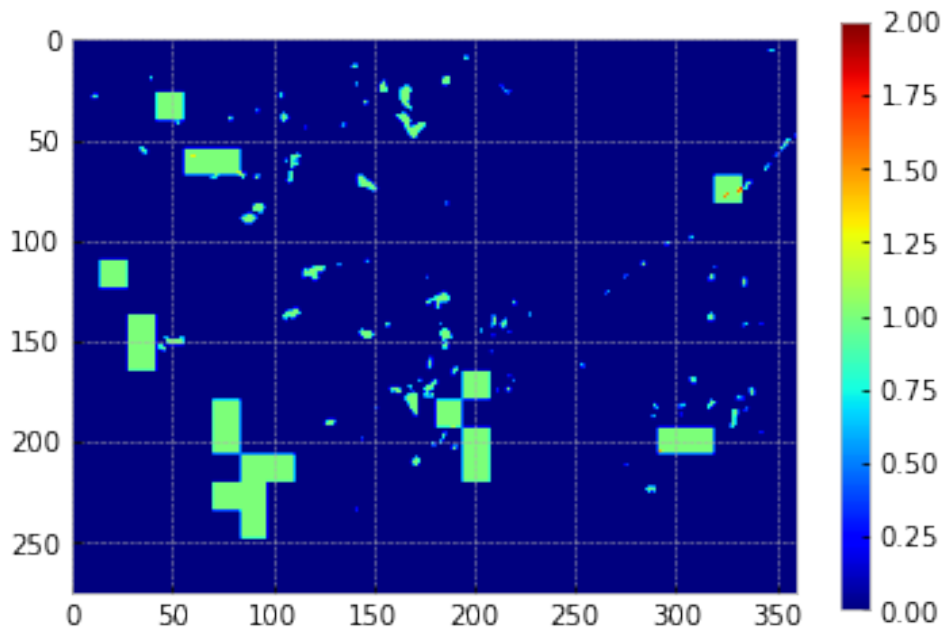


Figure 4.29: Error map of the satellite prediction over validation data (area 3). True positives are represented in red, True Negative in blue and misclassified pixels in green

The error map in Figure 4.29 highlights the aforementioned issue, as it shows that a single PRISMA pixel is bigger than the actual spot to be detected.

To show how the size of the unhealthy tree zones is impacting the prediction, the error map of the training data is reported in Figure 4.30.

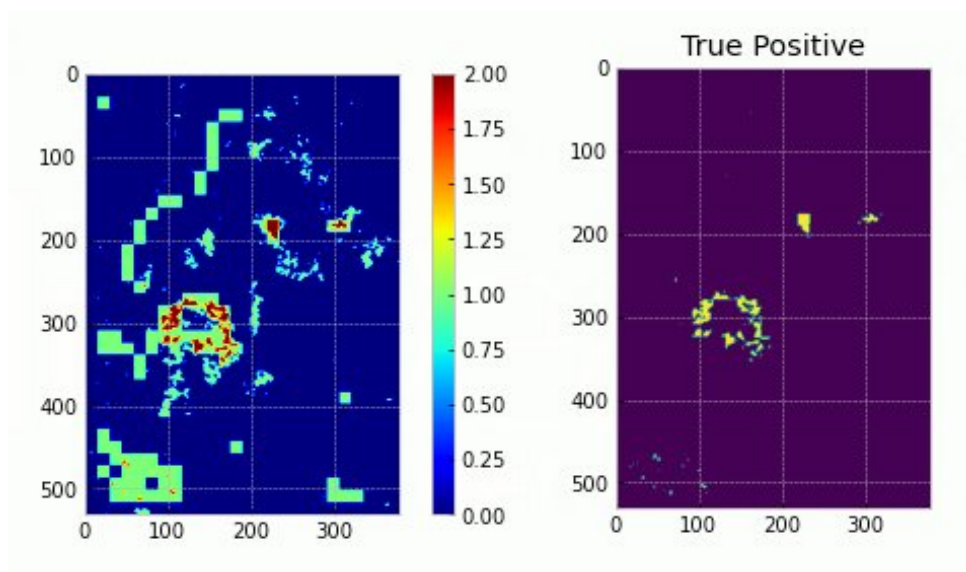


Figure 4.30: On the left, the error map of satellite prediction over training data (area 5). On the right, detected true positive over training data (area 5)

This map has no validation purposes, as it corresponds to the data used for training, but it is effective to show how, depending on the size, wider areas of risk may be detected by the algorithm. In this area (area 5), the percentage of unhealthy pixels rises up only to the 4%, but its effects on the prediction are still significantly high, as the algorithm is able to reach a precision level of the 12% (almost ten times higher than the area 3 one).

5 | Conclusions and future improvements

Given the results obtained from the current study, it can be stated that it has been possible to realize a new framework analysis, capable of detecting the potential effects of Bark Beetle attacks on trees from satellite Hyperspectral imagery on large infested areas. Moreover, the vegetation indexes extracted from the satellite reflectance have proven to be effective to achieve the aforementioned premise.

Nevertheless, due to an inevitable loss in spatial resolution because of the PRISMA sensor limitations, this solution cannot fully replace, in its current implementation, the function of aerial and ground surveys. This analysis has indeed proven that the Unmixing techniques can definitively improve the detection of trees' crowns, but the effects of a coarser resolution will eventually return to affect results in the spectral index extraction phase. As acknowledged in Chapter 4, a spatial resolution of 30m is far wider than the diameter of a single tree, which makes a single pixel not capable of detecting sharp changes between one tree and the other one. Because of this, the algorithm is only able to discover larger damaged areas. Concerning this point, it is important to underline that the model has been trained on a single image of 0.8 km², but it is able to recognize larger attacks on a 1721 km² size image. This bodes well for the future as it paves the way to a significant improvement, that can be brought by further analysis with more and larger training datasets.

However, training data is not the only source of data improvement, as also validation data has shown its limits. As anticipated in Chapter 4, the population of unhealthy trees in the validation area was almost absent and scattered under the pixel level, making it almost impossible to be detected by the algorithm. Therefore, it is worth saying that data availability played a crucial role in the outcome of the study.

Finally, it can be concluded that this satellite analysis cannot obviously substitute the accuracy and effectiveness of a pre-scheduled aerial survey, nor eliminate the costs of such a fundamental procedure, but it can be used as an important instrument to reduce the survey expenses, allowing to perform more qualitative analysis and optimize the planning

of aerial surveys, by inspecting larger land extensions and limiting the survey to the most likely vulnerable areas detected by the PRISMA satellite.

During the development of this study, the weaknesses and strengths of the model have been highlighted. In the following list, a set of useful hints has been drafted to pave the way for future further research in the field and possibly improve the outcomes of our analysis:

- first of all, since the shadow abundance map is including a large portion of trees' canopy (Figure 4.9), it can be evaluated to unify under the same class water and shadow, considering the similarity of their spectral signatures (observable in Figure 4.8 and 4.9). This can possibly improve the outline of trees' crowns by reducing the number of classes detected in the Unmixing phase
- as anticipated in Chapter 2, Unmixing can improve the detection of unhealthy vegetation, but the created abundance map are not taking into account the spatial distribution of every single abundance inside a PRISMA pixel. A further development can be the implementation of a super-resolution Hyperspectral satellite image, using one of the techniques presented in the State of the Art Chapter. By creating an image at high spectral and spatial resolution, the algorithm can surely deal with the local effects caused by the high resolution of validation data, and produce reliable results also in the validation step
- it could be evaluated the possibility to build a Machine Learning model, trained on the results of the current study, able to discriminate between healthy or infested trees. In a later stage, once the model will be properly trained and validated, it will be possible to ignore completely aerial data and classify the interested vegetation, using satellite data as the only input. This will allow to completely spare the planning and execution of complex aerial missions (as well as totally eliminating survey costs)

Bibliography

- [1] H. Abdullah, A. K. Skidmore, R. Darvishzadeh, and M. Heurich. Timing of red-edge and shortwave infrared reflectance critical for early stress detection induced by bark beetle (*ips typographus*, l.) attack. *International Journal of Applied Earth Observation and Geoinformation*, 82:101900, 2019.
- [2] J. Acker, R. Williams, L. Chiu, P. Ardanuy, S. Miller, C. Schueler, P. W. Vachon, and M. Manore. Remote sensing from satellites. 2014.
- [3] F. Amiri and M. H. Kahaei. Using spatial correlation in semi-supervised hyperspectral unmixing under polynomial post-nonlinear mixing model. *arXiv preprint arXiv:1803.00873*, 2018.
- [4] V. Bárta, P. Lukeš, and L. Homolová. Early detection of bark beetle infestation in norway spruce forests of central europe using sentinel-2. *International Journal of Applied Earth Observation and Geoinformation*, 100:102335, 2021.
- [5] J. M. Bioucas-Dias. A variable splitting augmented lagrangian approach to linear spectral unmixing. In *2009 First workshop on hyperspectral image and signal processing: Evolution in remote sensing*, pages 1–4. IEEE, 2009.
- [6] S. Cogliati, F. Sarti, L. Chiarantini, M. Cosi, R. Lorusso, E. Lopinto, F. Miglietta, L. Genesio, L. Guanter, A. Damm, et al. The prisma imaging spectroscopy mission: Overview and first performance analysis. *Remote sensing of environment*, 262:112499, 2021.
- [7] M. Dalponte, Y. T. Solano-Correa, L. Frizzera, and D. Gianelle. Mapping a european spruce bark beetle outbreak using sentinel-2 remote sensing data. *Remote Sensing*, 14(13):3135, 2022.
- [8] V. De Micco, A. Balzano, E. A. Wheeler, and P. Baas. Tyloses and gums: a review of structure, function and occurrence of vessel occlusions. *IAWA journal*, 37(2):186–205, 2016.
- [9] O. Eches, N. Dobigeon, and J.-Y. Tourneret. Enhancing hyperspectral image unmix-

- ing with spatial correlations. *IEEE Transactions on Geoscience and Remote Sensing*, 49(11):4239–4247, 2011.
- [10] A. Fernandez-Carrillo, Z. Patočka, L. Dobrovolný, A. Franco-Nieto, and B. Revilla-Romero. Monitoring bark beetle forest damage in central europe. a remote sensing approach validated with field data. *Remote Sensing*, 12(21):3634, 2020.
- [11] A. C. Foster, J. A. Walter, H. H. Shugart, J. Sibold, and J. Negron. Spectral evidence of early-stage spruce beetle infestation in engelmann spruce. *Forest Ecology and Management*, 384:347–357, 2017.
- [12] J. M. Frank, W. J. Massman, B. E. Ewers, L. S. Huckaby, and J. F. Negrón. Ecosystem co₂/h₂o fluxes are explained by hydraulically limited gas exchange during tree mortality from spruce bark beetles. *Journal of Geophysical Research: Biogeosciences*, 119(6):1195–1215, 2014.
- [13] R. P. Ghimire, M. Kivimäenpää, M. Blomqvist, T. Holopainen, P. Lyytikäinen-Saarenmaa, and J. K. Holopainen. Effect of bark beetle (*ips typographus* l.) attack on bark voc emissions of norway spruce (*picea abies karst.*) trees. *Atmospheric Environment*, 126:145–152, 2016.
- [14] C. Gomez and P. Lagacherie. Mapping of primary soil properties using optical visible and near infrared (vis-nir) remote sensing. In *Land surface remote sensing in agriculture and forest*, pages 1–35. Elsevier, 2016.
- [15] D. F. Gomez, H. M. Ritger, C. Pearce, J. Eickwort, and J. Hulcr. Ability of remote sensing systems to detect bark beetle spots in the southeastern us. *Forests*, 11(11):1167, 2020.
- [16] D. Hong, J. Yao, D. Meng, N. Yokoya, and J. Chanussot. Decoupled-and-coupled networks: Self-supervised hyperspectral image super-resolution with subpixel fusion. *arXiv preprint arXiv:2205.03742*, 2022.
- [17] A. Huete. Remote sensing for environmental monitoring. In *Environmental monitoring and characterization*, pages 183–206. Elsevier, 2004.
- [18] M. Kremezi, V. Kristollari, V. Karathanassi, K. Topouzelis, P. Kolokoussis, N. Taggio, A. Aiello, G. Ceriola, E. Barbone, and P. Corradi. Pansharpening prisma data for marine plastic litter detection using plastic indexes. *IEEE Access*, 9:61955–61971, 2021.
- [19] W. A. Kurz, C. Dymond, G. Stinson, G. Rampley, E. Neilson, A. Carroll, T. Ebata,

- and L. Safranyik. Mountain pine beetle and forest carbon feedback to climate change. *Nature*, 452(7190):987–990, 2008.
- [20] C. Lanaras, E. Baltsavias, and K. Schindler. Hyperspectral super-resolution with spectral unmixing constraints. *Remote Sensing*, 9(11):1196, 2017.
- [21] D. D. Lee and H. S. Seung. Learning the parts of objects by non-negative matrix factorization. *Nature*, 401(6755):788–791, 1999.
- [22] A. J. Meddens, J. A. Hicke, L. A. Vierling, and A. T. Hudak. Evaluating methods to detect bark beetle-caused tree mortality using single-date and multi-date landsat imagery. *Remote Sensing of Environment*, 132:49–58, 2013.
- [23] K. C. Mertens, B. De Baets, L. P. Verbeke, and R. R. De Wulf. A sub-pixel mapping algorithm based on sub-pixel/pixel spatial attraction models. *International Journal of Remote Sensing*, 27(15):3293–3310, 2006.
- [24] J. M. Nascimento and J. M. Dias. Vertex component analysis: A fast algorithm to unmix hyperspectral data. *IEEE transactions on Geoscience and Remote Sensing*, 43(4):898–910, 2005.
- [25] A. Pisanti, S. Magrì, I. Ferrando, and B. Federici. Sea water turbidity analysis from sentinel-2 images: Atmospheric correction and bands correlation. *ISPRS-International Archives of the Photogrammetry, Remote Sensing and Spatial Information Sciences*, 48:371–378, 2022.
- [26] A. Plyer, E. Colin-Koeniguer, and F. Weissgerber. A new coregistration algorithm for recent applications on urban sar images. *IEEE Geoscience and Remote Sensing Letters*, 12(11):2198–2202, 2015.
- [27] S.-E. Qian. Hyperspectral satellites, evolution, and development history. *IEEE Journal of Selected Topics in Applied Earth Observations and Remote Sensing*, 14:7032–7056, 2021.
- [28] E. Vangi, G. D’Amico, S. Francini, F. Giannetti, B. Lasserre, M. Marchetti, and G. Chirici. The new hyperspectral satellite prisma: Imagery for forest types discrimination. *Sensors*, 21(4):1182, 2021.
- [29] X. Xu, X. Tong, A. Plaza, Y. Zhong, H. Xie, and L. Zhang. Using linear spectral unmixing for subpixel mapping of hyperspectral imagery: A quantitative assessment. *IEEE Journal of Selected Topics in Applied Earth Observations and Remote Sensing*, 10(4):1589–1600, 2016.

- [30] X. Xu, J. Li, C. Wu, and A. Plaza. Regional clustering-based spatial preprocessing for hyperspectral unmixing. *Remote Sensing of Environment*, 204:333–346, 2018.
- [31] N. Yokoya, T. Yairi, and A. Iwasaki. Coupled nonnegative matrix factorization unmixing for hyperspectral and multispectral data fusion. *IEEE Transactions on Geoscience and Remote Sensing*, 50(2):528–537, 2011.
- [32] N. Yokoya, C. Grohnfeldt, and J. Chanussot. Hyperspectral and multispectral data fusion: A comparative review of the recent literature. *IEEE Geoscience and Remote Sensing Magazine*, 5(2):29–56, 2017.
- [33] F. Zemek. *Airborne remote sensing: theory and practice in assessment of terrestrial ecosystems*. Global Change Research Centre AS CR, 2014.

List of Figures

1.1	Geographical distribution of the study area and the extent of the two sensor acquisitions. In red it is possible to appreciate the Gadertal study area outline, in blue the PRISMA image outline and in green the airborne acquisitions with their corresponding area number in black	3
2.1	Visual representation of the three neighbourhood models as a function of the scale factor S. Credits: [23].	15
3.1	Area 5 classification map provided by the AVT AS company	18
3.2	Area 3 classification map provided by the AVT AS company	19
3.3	A visual representation of PRISMA and AisaFENIX" bandset; each segment represents a sensor band (wavelengths in nanometers) for the Aerial, PRISMA and PRISMA reduced hyperspectral cube (the latter is a PRISMA cube with a cut on the last 15 bands, to match the same final wavelength of the aerial sensor, as it will be further explained in the next chapters) . .	20
3.4	RGB representation of PRISMA's study area. The pixel coordinates are represented on the x and y axis (as for all the other following images) . . .	21
3.5	RGB representation of aerial study area (area 5)	21
3.6	RGB representation of aerial study area (area 3)	22
3.7	legend workflow schema	23
3.8	pre-processing workflow schema	23
3.9	unmixing workflow schema	27
3.10	Training regions of interest for the unmixing procedure	29
3.11	Visual representation of the "pairing array" extraction	31
3.12	Mean and standard deviation of pure PRISMA healthy Spruce trees' spectral signatures. The solid lines represent the mean of the 9 spectral signatures of PRISMA and the 1924 ones of asiaFENIX, while the transparent area around it, identifies the standard deviation of the same endmembers .	32

3.13	Mean and standard deviation of pure asiaFENIX healthy Spruce trees' spectral signatures. The solid lines represent the mean of the 9 spectral signatures of PRISMA and the 1924 ones of asiaFENIX, while the transparent area around it, identifies the standard deviation of the same endmembers	32
3.14	Vegetation Index Extraction workflow schema	33
3.15	Frequency analysis workflow schema	36
3.16	Frequency analysis workflow schema	37
4.1	The set of 7 tie points selected for image coregistration on PRISMA image	40
4.2	The set of 7 double points selected for image coregistration on asiaFENIX image	40
4.3	Before and after representation of the satellite image coregistration	41
4.4	Healthy tree spectral signature of aerial sensor and PRISMA band paired version. The blue curve is used to represent the satellite signature, while green is used for the aerial one	43
4.5	Unhealthy tree spectral signature of aerial sensor and PRISMA band paired version. The blue curve is used to represent the satellite signature, while green is used for the aerial one	44
4.6	Unvegetated area spectral signature of aerial sensor and PRISMA band paired version. The blue curve is used to represent the satellite signature, while green is used for the aerial one	45
4.7	Grassland spectral signature of aerial sensor and PRISMA band paired version. The blue curve is used to represent the satellite signature, while green is used for the aerial one	46
4.8	Water spectral signature of aerial sensor and PRISMA band paired version	46
4.9	Shadow spectral signature of aerial sensor and PRISMA band paired version. The blue curve is used to represent the satellite signature, while green is used for the aerial one	47
4.10	PRISMA abundance maps of the entire 30km ² acquisition tile	48
4.11	PRISMA abundance maps of area 5	48
4.12	PRISMA abundance of area 3	49
4.13	PRISMA binary maps of trees (healthy and unhealthy together) before and after sieving	50
4.14	PRISMA binary maps of trees (healthy and unhealthy together) of area 3 .	50
4.15	PRISMA binary maps of trees (healthy and unhealthy together) of area 5 .	51
4.16	Binary mask of healthy trees of area5, extracted from aerial data for training purposes	52

4.17	binary mask of unhealthy trees of area 5, extracted from aerial data for training purposes	52
4.18	NDVI aerial vegetation maps example used for training	53
4.19	CLRE and GNDVI values distribution for healthy and unhealthy trees in random sample	54
4.20	NBRI and NDREI values distribution for healthy and unhealthy trees in random sample	54
4.21	NDVI and NRVI values distribution for healthy and unhealthy trees in random sample	54
4.22	SLAVI values distribution for healthy and unhealthy trees in random sample	55
4.23	PRISMA vegetation index maps binarized with the threshold. In black are represented pixels exceeding the threshold (pixels with a higher risk of being unhealthy trees) and in white healthy trees or pixels masked out by the trees mask	56
4.24	On the left side, the frequency map of unhealthy trees, where each pixel value corresponds to the number of indexes that exceeded the threshold in the spectral index analysis. On the right side, the binarized frequency map, where black pixels correspond to the 39% of the pixels with the highest frequency.	57
4.25	On the left side, frequency map of unhealthy trees in area 5, where each pixel value corresponds to the number of indexes that exceeded the threshold in the spectral index analysis. On the right side, the binarized frequency map, where black pixels correspond to the 39% of the pixels with the highest frequency.	58
4.26	On the left side, frequency map of unhealthy trees in area 3, where each pixel value corresponds to the number of indexes that exceeded the threshold in the spectral index analysis. On the right side, the binarized frequency map, where black pixels correspond to the 39% of the pixels with the highest frequency.	58
4.27	On the left, resampled PRISMA frequency binary map. On the right, aerial validation binary map (area 3)	59
4.28	Confusion matrix of the satellite prediction over the validation area (area 3)	60
4.29	Error map of the satellite prediction over validation data (area 3). True positives are represented in red, True Negative in blue and misclassified pixels in green	61
4.30	On the left, the error map of satellite prediction over training data (area 5). On the right, detected true positive over training data (area 5)	61

List of Tables

2.1	Infrared indexes' involved spectral bands with their formulas	6
2.2	Red-edge indexes' involved spectral bands with their formulas	7
2.3	Leaf and water indexes' involved spectral bands with their formulas	8
2.4	Moisture and drought indexes' involved spectral bands with their formulas	9
2.5	Tasseled cap indexes' involved spectral bands with their formulas	10
2.6	Other spectral indexes' involved spectral bands with their formulas	10
3.1	Satellite and aerial image information	20
4.1	Pixel mean error for each transformation type (pixel units)	41
4.2	Threshold selected for each index vegetation map binarization	55

